

LA-5906

e. 3

CIC-14 REPORT COLLECTION  
**REPRODUCTION  
COPY**

UC-32 and UC-45  
Reporting Date: March 1975  
Issued: July 1975

## Numerical Calculation of the Cylinder Test

by

W. Fickett  
L. M. Scherr\*



\*Present address: Biomedical Division, Lawrence Livermore Laboratory,  
P. O. Box 808, Livermore, CA 94550



An Affirmative Action/Equal Opportunity Employer

Printed in the United States of America. Available from  
National Technical Information Service  
U S Department of Commerce  
5285 Port Royal Road  
Springfield, VA 22151  
Price: Printed Copy \$4.00 Microfiche \$2.25

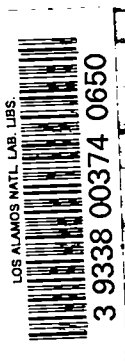
This report was prepared as an account of work sponsored by the United States Government. Neither the United States nor the United States Energy Research and Development Administration, nor any of their employees, nor any of their contractors, subcontractors, or their employees, makes any warranty, express or implied, or assumes any legal liability or responsibility for the accuracy, completeness, or usefulness of any information, apparatus, product, or process disclosed, or represents that its use would not infringe privately owned rights.

## GLOSSARY

HE - high explosive  
JWL - Jones, Wilkins, and Lee (equation of state)  
MAGEE and HEMP - LASL and LLL mesh codes, respectively.  
Mesh calculation or code - using the Lagrangian method where each (ordinarily quadrilateral) computation cell represents a fluid element  
MOC - method of characteristics

## SYMBOLS

sub o initial state  
D detonation velocity  
e internal energy concentration (per unit mass)  
 $\gamma$  adiabatic exponent; at Chapman-Jouguet state for HE:  $\gamma = \rho_0 D^2/p - 1$   
sub J Chapman-Jouguet state for HE  
L distance from initiating plane  
 $\lambda$  HE degree of reaction ( $\lambda = 0$  for no reaction,  $\lambda = 1$  for complete reaction)  
p pressure  
Q HE heat of reaction  
r radial coordinate  
R -  $R_0$  wall displacement (outer surface)  
 $\rho$  mass density  
t time  
u lateral wall velocity  
v specific volume,  $1/\rho$   
z longitudinal coordinate



## NUMERICAL CALCULATION OF THE CYLINDER TEST

by

W. Fickett and L. M. Scherr

### ABSTRACT

The cylinder test evaluates high explosive performance in short-time applications. We study the accuracy of its calculation by a two-dimensional (time-dependent) Lagrangian mesh code. The principal comparison is made with a more accurate calculation of the steady flow near the front by the method of characteristics.

Refining the computation mesh produces a surprising artifact: a large pressure bump on the axis produced by a spurious conical wave originating at the detonation front's edge. Nevertheless, the quantities of interest, late wall displacement and velocity, are accurately calculated. With 13 lateral computation cells, after 10 mm of wall motion the error in arrival time is +0.07  $\mu$ s, and the error in mean velocity, which fluctuates from reverberations, is less than 0.03 mm/ $\mu$ s.

### I. INTRODUCTION

The cylinder test is commonly used to evaluate HE performance when propelling metal shells over  $\sim 10 \mu$ s.<sup>1</sup> It has also been used to study less homogeneous explosives with longer reaction times.<sup>2</sup> As part of a project to evaluate detonating explosives models used in numerical hydrodynamics calculations, we studied the accuracy of a two-dimensional (time-dependent) Lagrangian mesh code calculation of the cylinder test, extending the results of Wilkins.<sup>3</sup>

We compared the results from the Los Alamos Scientific Laboratory (LASL) mesh code MAGEE with a steady-state calculation by the more accurate method of characteristics (MOC),<sup>4</sup> calculations made with the similar Lawrence Livermore Laboratory (LLL) code HEMP,<sup>5</sup> and some features from a precise LASL experiment.<sup>6</sup> The main results were

- (1) As the calculation mesh is refined below the typical size (13 lateral cells) of routine calculations, a surprising artifact appears. A spurious conical wave that starts at the front's edge in the HE propagates along the tail of the Prandtl-Meyer rarefaction attached to the front, and

converges to produce a pressure peak on the axis, where the pressure as a function of longitudinal distance should have a plateau at less than half this value. This artifact seems to be typical in some mesh codes of this type.

- (2) Despite this unpleasant artifact, the calculated wall position and local mean wall velocity (averaged over reverberations) are accurately calculated and have a reasonable mesh size dependence. With 13 lateral cells, the error in arrival time after the wall has moved 10 mm is +0.07  $\mu$ s in the standard geometry of 15.4-mm initial outer radius. The error in mean wall velocity at this displacement is approximately zero. Its sign is difficult to determine because of the irregularity of the calculated reverberations, whose peak-to-peak amplitude is 0.25 mm/ $\mu$ s, but its magnitude is probably  $< 0.03$  mm/ $\mu$ s. With so few cells, the early wall motion is off: the calculated mean velocity over the first reverberation is about 8% too high.

## II. CONFIGURATION AND TYPICAL RESULTS

Figure 1 shows the cylinder test geometry<sup>1</sup> and a typical experimental wall motion.<sup>7</sup> Some characteristic values for the explosive PBX 9404 are given in Table I, in which L is the distance from the left end of the test HE and R is the outer wall radius. Most of the values are for a transverse wall displacement  $R - R_0$  of 20 mm, as shown on the left-hand side of the dynamic view in Fig. 1. The flow becomes steady (in a frame attached to the front) when the front has traversed about four HE diameters. The quantity usually measured is wall displacement vs time at fixed L. The quantity  $\bar{\rho}$  in Table I is the mean mass density over the cross section when the wall at the measuring station has reached this expansion.

## III. PROPERTIES OF THE MOTION

Our calculational model assumes the usual, simplest detonation model. The reaction is instantaneous; the front is plane and moves at the (constant) Chapman-Jouguet velocity, with sonic flow directly behind it.

We compared our calculation with those in Ref. 4, which used the more accurate method of characteristics (MOC). It makes the additional assumption that the flow is steady in a frame attached to the front. We use its results to display some of the physics of the problem. This calculation was done for both slab and cylindrical geometry. First we discuss the simpler slab case, which is a slab of HE between two flat metal plates. The side and rear boundary conditions are  $p = 0$ , thus the flow is supersonic everywhere behind the detonation front.

With these assumptions, the results scale in lateral size. At fixed time, any dependent variable  $q$  of the flow field may be written as

$$q = f(r, z_f - z) ,$$

where  $z_f$  is the position of the front. For an observer of the wall at fixed  $z$

$$q = g(t); t = (z_f - z)/D .$$

If all radial dimensions are increased by  $k$ , we have

$$q = [f kr, k(z - z_f)/D]$$

and for the observer at fixed  $z$

$$q = g(t); t = k(z - z_f)/D .$$

### A. Slab

Figure 2a shows the  $r$ - $z$  diagram. A centered Prandtl-Meyer rarefaction wave propagates from each intersection of the front with the wall. Only the tail characteristic of the fan is shown. The situation is complicated by the interaction of these two rarefactions. If the HE were laterally semi-infinite, so that there were only one rarefaction, the

TABLE I

### TYPICAL CYLINDER TEST

#### Distance, time

measurement at fixed  $L = 248$  mm (9.75 in.), and at

wall displacement  $r = 20$  mm (values below are for this displacement)

in time  $t = 12.6$   $\mu$ s (from first motion)

wall velocity at  $R - R_0 = 0$  mm:  $u = 0.84$  mm/ $\mu$ s

$R - R_0 = 5$  mm:  $u = 1.5$  mm/ $\mu$ s

$R - R_0 = 20$  mm:  $u = 1.7$  mm/ $\mu$ s

as wall moves 20 mm, front moves 110 mm

#### Mass, energy

wall mass per HE mass = 2.19

late wall energy per HE chemical energy  $\approx 0.5$

#### Mean state at $R - R_0 = 20$ mm

$\bar{\rho}/\rho_0 = 1/7$ ;  $p(\bar{\rho}/\rho_0) \approx 70$  MPa

on axis:  $p \approx 70$  MPa

at wall:  $\bar{p} \approx 0$  (fluctuating from reverberations)

#### Experimental error<sup>7</sup> (standard deviations)

$\sigma_t = 0.5\%$  (= 0.063  $\mu$ s at  $r = 20$  mm)

$\sigma_u = 1\%$  (= 0.017 mm/ $\mu$ s at  $r = 20$  mm)

#### Explosive,<sup>7</sup> PBX 9404

$\rho_0 = 1.840$  Mg/m<sup>3</sup>,  $D = 8.8$  mm/ $\mu$ s,  $p = 37$  GPa,  $\gamma = 2.85$

characteristics issuing from the corner would be straight lines and each would have a constant state along it.

The shock in the copper stands at the matching angle. A centered rarefaction moves back from its intersection with the free surface and reverberates in the plate in the usual way, where the outward-facing waves are compressions and the inward-facing waves are rarefactions. The first region behind the tail of the Prandtl-Meyer waves is nearly constant and is changed only by the Prandtl-Meyer wave from the opposite boundary. Some of the characteristics from the lower Prandtl-Meyer wave are only sketched in because the code's output list gives only their intersections with the center line and the HE/copper interface. The characteristics are strongly refracted and spread apart; all those shown originate within a very small angle at the lower corner and thus carry a small range of pressure. The pressure at point A,  $0.641 p_j$ , is only 0.5% below that at point O. This pressure change is reduced further by reflection at the interface, so that the axis pressure is constant at  $p = 0.449 p_j$  to eight figures between points B and C. Figure 2b shows the axial pressure profile. The regions of decreasing pressure are caused by the front Prandtl-Meyer wave and by the subsequent rarefactions from the free surface. Pressure profiles vs lateral position are shown in Fig. 2c. Their structure is easily correlated with the x-t diagram. Again we see that the departures from the case of semi-infinite HE are small; for example, in that case there would be no change in pressure beyond point X on the  $z/r_E = 0.5$  profile.

#### B. Cylinder

The cylinder case shows the effects of radial convergence. The initial slope of the characteristics in the corner of the Prandtl-Meyer waves is unchanged, but they are now curved not only because of interaction with the wave from the opposite side of the tube but also because of the cylindrical geometry. The radial convergence not only lowers the first plateau pressure considerably from 0.41 to  $0.14 p_j$  but also moves the plateau to the rear and widens it from BC to B'C' in Fig. 2c.

The output list does not contain sufficient information to construct an x-t diagram like that in

Fig. 2a, but the general effect is seen by considering the displacement and lengthening of the central plateau. The characteristic from point B' reaches the inner wall of the copper at  $z/r_E = 8.22$ ,  $r/r_E = 2.25$ . Figure 3 shows three pressure profiles vs lateral distance; pressure vs longitudinal distance will be shown in Sec. V.

#### C. Tail Wave

A flash x-ray photograph<sup>8</sup> of the slab case, Fig. 4, shows prominent lines that indicate a density bump lying approximately along the tail characteristic of the Prandtl-Meyer wave. These lines are misleadingly prominent; detailed examination shows that the film density rise from local minimum to local maximum is only about  $0.075 \text{ Mg/m}^3$ . Other x-ray photographs of similar configurations show this phenomenon with varying degrees of prominence; in some it is absent. Assuming it is "real," i.e., not caused, for example, by something like an air gap or hardened surface layer on the copper, it could arise in one of two ways. First, with a sufficient change in the copper and HE equations of state, the pressure-angle rarefaction and shock loci (polars) could cross in a way that would indicate the formation of a small shock building up along the tail of the rarefaction. Second, an HE reaction zone of appreciable length might produce this effect. We know of no detailed study of this problem, but many schlieren photographs of gas detonations, such as that shown in Fig. 5,<sup>9</sup> show similar prominent waves coming from the edge. Of course in the gas there may be more of a boundary layer effect, but the walls are incompressible. In our case, we do not know how important this boundary layer may be.

The MAGEE calculation, with its artificial viscosity, has a finite shock thickness. For similar numerical reasons, the chemical reaction must occur over several time steps in the calculation, giving rise to a small but finite reaction zone. With sufficiently fine zoning, the calculation shows, as mentioned earlier, a spurious conical wave propagating in along the tail of the Prandtl-Meyer rarefaction. Perhaps this tells us that physically we should expect such a disturbance when the front has a finite thickness.

#### IV. ADJUSTABLE PARAMETERS

Here we consider the unavoidable intrusion of the adjustable parameters (dials) of our calculational tool. These fall into two categories. When comparing with another calculation or an exact solution, the constitutive relations are not in question; however, we are concerned with the numerical-method dials, such as the computation-cell size and shape and the form and amount of artificial viscosity. To compare with experiment, we also have to know whether we have the right constitutive relations.

Appendix A describes the main features of the MAGEE code, the dials and options that must be set, and some of the problems of using it.

The MOC calculation<sup>4</sup> with which we compare makes several assumptions. The front in the HE is a plane surface of discontinuity in which reaction is completed instantaneously. It moves at (plane) Chapman-Jouguet velocity, so that the flow directly behind it is sonic. The flow is steady in the frame attached to the shock; one consequence of this is that it is everywhere supersonic behind the front, so that the rear boundary condition (essentially ambient pressure) does not explicitly enter the calculation. Finally, the copper is treated as a fluid. With the exception of omitting the material strength of the copper, these assumptions are probably quite good for the real system.

The main numerical-method dials and switches are

- (1) computation-cell size, shape, and distribution,
- (2) form and amount of artificial viscosity,
- (3) whether or not to allow slip at the HE and copper interface,
- (4) method of "burning the explosive," i.e., of propagating the detonation, and
- (5) particular set of difference equations used.

Further, for this application, where we run a time-dependent calculation until it becomes steady, we must ensure that the detonation has run far enough so that a steady state is achieved and also that the rear boundary condition used in the calculation has a negligible effect on the results.

We have not made a systematic quantitative study of the effect of cell shape or distribution,

but some results are given in the axial-pressure-bump artifact discussion (Sec. V). We also discuss our comparison of longitudinally graduated and uniform meshes in Sec. V.

We generally used the standard (default) artificial viscosity, which is the Richtmyer-von Neumann quadratic form described in Appendix A. Different viscosity forms and amounts were used in the pressure-bump study.

The method of propagating the detonation, described in Appendix A, consists of programming a plane initiation front to move at the Chapman-Jouguet detonation velocity. Reaction is initiated in each particle when it passes into this front and proceeds rapidly at a constant rate to completion. The reaction time is normally the time required for the detonation front to cross one computation cell. With this method, the peak pressure at the front does not become steady until the front has traversed ~50 cells. An example of a steady axial-pressure profile is given in Sec. V. The HEMP code uses a different recipe for propagating the detonation. HEMP gives lateral pressure profiles near the front that fall off less rapidly toward the edges than the ones in our MAGEE code.

The form of the difference equations is not a built-in adjustable parameter of the program. However, we were so disturbed by the axial-pressure bump that we modified the program to try the "Green's transformation" acceleration equations (see Appendix A); this made little difference. The results, described in Sec. V, are qualitatively similar in all cases.

To compare with the MOC calculation, we must achieve steady flow. Steady flow to 20 mm of wall displacement is achieved between three ( $L = 75$  mm) and four ( $L = 100$  mm) HE diameters from initiation. In one set of experiments,<sup>7</sup> the time for a 20-mm wall displacement changes by 0.1  $\mu$ s or 1% between  $L = 75$  mm and  $L = 100$  mm, and by smaller amounts beyond  $L = 100$  mm. In another experiment,<sup>6</sup> no systematic difference could be detected between  $L = 170$  and  $L = 250$  mm, which is the standard measurement station. At  $L = 120, 140, 160,$  and  $180$  mm, our calculated times varied by <1 part in 10 000 for 10 mm of wall motion and by <1 part in 1 000 for 20 mm. We thus achieve steady flow, but at a significant cost in calculation time.

As expected, the exact choice of the rear boundary condition has little effect; we generally used a continuative rear boundary. Changing to a rigid rear boundary (a severe perturbation that prevents all backward motion of the detonation products across the initiating plane) changed the time for a 20-mm wall displacement at  $L = 100$  mm by  $<1$  part in 20 000.

The cylinder test is generally used to determine the HE equation of state; therefore, we are not concerned here with uncertainties in its equation of state. In performing this calibration, it would be desirable to know the properties of the copper case. How serious are errors here? We expect the hydrostatic part of the equation of state to make little difference at late times because the case pressure rapidly drops to zero. The principal confinement agency is the mass of the case, with some contribution from the hoop strength of the material. In one set of calculations,<sup>7</sup> replacing the copper by the same mass of ductile steel increased the 20-mm displacement time by only 1%; replacing the ductile steel by mild steel increased the time over that for copper by 2.8%; and increasing the yield strength of the copper from  $Y_0 = 0.3$  GPa to  $Y_0 = 1$  GPa increased the calculated time by 1.3%. We repeated this last comparison and got 1.1%.

## V. RESULTS

We have presented data analysis and display details in Appendix B, calculation specifications in Appendix C, and data tables in Appendix D. In all of our calculations, we used the description "10 + 3 lateral cells" to mean 10 lateral cells in the HE and 3 in the copper. Where the mesh is refined to "20 + 6 lateral cells," the longitudinal cell dimension is also halved so that the cells retain their shape. All results are presented as seen by an observer at fixed  $z$ , with wall displacement as the independent variable.

### A. Mesh Calculations vs MOC

Figure 6 shows the axial pressure vs distance behind the front. All of the calculations except the upper solid curve discussed below have been carried to a steady state. The front positions for MAGEE coarse, MAGEE fine, and HEMP are  $L = 285$ , 162, and 97 mm, respectively. The true solution (MOC calculation) has the plateau discussed in the previous

section. The coarse (10 + 3 lateral cells) MAGEE calculation shows the typical blunting at the front due to artificial viscosity, with the peak pressure down to about 85% of its true value. The mesh is coarse enough to smooth the plateau details, but agreement farther to the rear is good. The surprise comes when the mesh is refined. For the fine mesh (20 + 6 lateral cells) MAGEE calculation, the front pressure rises to 92% of the correct value and the fall toward the plateau is more nearly correct; however, there is a large hump in the middle of the plateau with a peak pressure that is over double the correct value. To keep this fine mesh calculation alive, we had to remove rear net sections closer to the front than we wished, with the result that the points shown are all we have. Also shown is a finer mesh (25 + 5 lateral cells) HEMP calculation run for us by E. L. Lee of LLL. Because this calculation is for a slightly different explosive (PBX 9404 described by the JWL equation of state instead of LX04-01 described by the Wilkins equation of state) and metal (copper with material strength), a quantitative comparison cannot be made; however, it gives the same spurious pressure peak. Brian Lambourne of the UK Atomic Weapons Research Establishment also ran calculations for us with that Laboratory's code (similar to MAGEE). His results were similar to ours.

We did many more calculations to study this phenomenon. Most of these calculations used our standard fine mesh, but with one less cell in the copper, i.e., 20 + 5 lateral cells, and square cells in the HE. We found that

- (1) The bump first appears early in the run. It is not present with the front at  $L = 35$  mm, but is clearly evident at  $L = 50$  mm. It becomes nearly steady at  $L = 100$  mm, with slight growth in peak pressure beyond this point.
- (2) Changing to slab geometry reduced but did not completely remove the bump, thus confirming the importance of cylindrical convergence.
- (3) Changing the HE equation of state from the Wilkins form to a simple  $\gamma$ -law had no effect.



- (4) Changing the rear boundary condition had no effect; free, continuative, and fixed rear boundaries were tried.
- (5) Replacing the MAGEE acceleration equations by the "Green's transformation" (HEMP) form gave similar results to the calculation with the HEMP code itself (Fig. 6), producing a small increase in peak pressure of the bump.
- (6) Reducing the lateral cell spacing in the copper by a factor of 4 had no effect, but reducing the copper density to  $0.1 \text{ Mg/m}^3$  eliminated the bump. These results suggest that some type of wall interaction is responsible.
- (7) Increasing the coefficient of the standard quadratic artificial viscosity flattened the bump and moved it away from the front. With a linear combination of linear and quadratic viscosities, increasing the coefficient of the linear part increased the peak pressure of the bump.
- (8) Halving only  $\Delta r$  in the HE increased the peak pressure of the bump, moved it toward the front, and added a second smaller bump near the back end of the plateau. Halving both  $\Delta r$  and  $\Delta z$  sharpened the bump, raised its peak pressure, and moved it toward the front. Halving  $\Delta r$  and doubling  $\Delta z$  flattened the bump and moved it away from the front. Recall that these changes also change the viscosity, which is proportional to cell area.

C. L. Mader has performed some additional calculations with his 2DL<sup>10</sup> and 2DE<sup>11</sup> codes. The 2DL code is a Lagrangian code patterned after MAGEE; 2DE is a newer Eulerian code. These calculations use a constant-pressure rear boundary condition with different values of the specified pressure, both sharp-shock and CJ-volume burns, and fine (20 + 4 lateral cells) and very fine (40 + 8 lateral cells) meshes. Most of them were carried to a front L of 35 to 45 mm. All of these show similar smoothly monotone profiles with no hint of a bump or plateau. One 2DL calculation with a sharp-shock burn, fine (20 + 4) mesh, and rear-boundary pressure of 4 GPa was carried to a front L of 63 mm. Its axial pressure profile, shown as the upper solid curve in Fig. 6,

appears to be forming a plateau, but lies well above the steady solution. The fine MAGEE calculation at the same front L (see item 1 in the variations above) has a profile not very different from the steady fine MAGEE curve of Fig. 6, with an obvious bump. We cannot explain this difference. Much more work is needed to understand the cause of this artifact.

We now consider the calculated wall motion. The three mesh calculations compared with MOC were the coarse (10 + 3) and fine (20 + 6) MAGEE calculations described above, and the finer mesh (32 + 6) HEMP calculation reported by Wilkins.<sup>3</sup> Unfortunately, the HEMP calculation extends to a displacement of only 5 mm. The choice of  $t_0$ , the time at which the wall motion begins, is described in Appendix B.

Figure 7 shows the early wall motion for MOC and the mesh calculations in various combinations. The complete wall motions are compared in Fig. 8. Figures 8c through 8l make comparisons at two magnifications by displaying differences of the calculated times  $\Delta t$  from the times given by a smooth reference curve

$$\Delta t = t_c(R) - t_r(R) \quad ,$$

where  $t_c$  is the time at R from the calculation in question, and  $t_r$  is the time from the reference curve at the same R. The two reference curves used are

1. linear

$$t = (R - R_0)/1.3$$

2. exponential (see Appendix B)

$$u_0 = 0.7912 \text{ mm}/\mu\text{s}$$

$$u_\infty = 1.551 \text{ mm}/\mu\text{s}$$

$$\hat{x} = 2.56 \text{ mm.}$$

The linear reference curve gives a magnification of ~14 times, and the exponential reference curve gives a magnification of ~35 times.

All of the mesh calculations show some irregularities in the reverberations, with the finer meshes giving more nearly the correct period, but with finer scale irregularities. The mean velocity is too large in the  $0 < x < 1$  range (the first reverberation), too small in the  $1 < x < 4$  range, and very nearly correct for  $x > 4$ . If we arbitrarily define the mean velocity over the first reverberation as the slope of the line in  $x-t$  joining the first two inflection points (initial point and first inflection point for MOC), we find percentage deviations for this mean velocity from MOC as follows. The mean velocity is determined in each case from the two points listed.

MOC	----	from points 1 and 9
Coarse MAGEE	+ 8.6%	from points 3 and 10
Fine MAGEE	+ 5.4%	from points 2 and 9
HEMP	+ 4.8%	from points 2 and 9

Figure 9 shows the wall velocities calculated by MAGEE and MOC (these are not given for the HEMP calculation). The coarse MAGEE shows fairly regular reverberations of about the right magnitude, a mean frequency about 15% low, and a curious flattening of some of the lower peaks. The fine MAGEE is puzzling because the reverberations become somewhat irregular. Once the initial transient is over, the envelope of the two MAGEE calculations agrees fairly well with MOC.

#### B. MAGEE vs HEMP and Experiment

Figure 10 compares more realistic MAGEE and HEMP calculations and two experiments. The results shown are for the HE PBX 9404-03. Both calculations used the JWL equation of state with the  $\Delta A$  parameters ( $p_j = 37.0$  GPa) given in Table II of Ref. 7. All results are presented as time differences from the exponential reference curve of Appendix B, with parameters

$$u_0 = 0.835 \text{ mm}/\mu\text{s}, u_\infty = 1.788 \text{ mm}/\mu\text{s}, \hat{x} = 3.58 \text{ mm}.$$

Because the JWL equation of state constants were determined by calibration to the LLL experiment, we expected and found that the HEMP calculation<sup>7</sup> closely reproduced that experiment. Although there is a late arrival time difference between the LASL<sup>6</sup> and LLL<sup>7</sup> experiments, which are about the same size

as the quoted LLL error, the velocity is similar after the first several millimeters of wall motion. The LASL points are as reported, with no smoothing. The LLL points are as reported in Ref. 7. The LLL experiment was one of a set covering many explosives; it did not attempt to look closely at the early motion. The LASL experiment was a single, high-precision effort with special attention given to the early motion.

The MAGEE calculation shows a late time velocity of about 1.5% less than HEMP and an arrival time velocity 0.16  $\mu\text{s}$  later. The arrival times were arbitrarily set equal at a 2-mm displacement (see Appendix B). We cannot account for this difference. Both calculations used the same HE equation of state. The computational net was identical toward the end of the stick; the HEMP net was longitudinally graduated as described in Ref. 7, whereas the MAGEE net was longitudinally uniform. Substituting the HEMP longitudinally graduated net in the MAGEE calculation increased the discrepancy: it made the arrival time at 20-mm displacement 0.025  $\mu\text{s}$  later while leaving the late time velocity unchanged. The other difference is in the copper description. MAGEE and HEMP used the same elastic-plastic model that had a yield strength  $Y_0$  of 0.3 GPa. The copper equation of state used in the HEMP calculation was not reported; we used the standard LASL copper equation of state described in Appendix C. Slight differences here as an explanation of the discrepancy are ruled out by the insensitivity to variations in the wall material (at constant cross-sectional mass) described in Sec. IV.

Figure 11 compares the early wall motion calculated by MAGEE with that measured in the LASL experiment. The difference is very nearly the same as that between the MAGEE and MOC calculations seen in Sec. V.A. Here the MAGEE velocity over the first reverberation is 8.3% higher than experiment, whereas (with the same mesh), MAGEE was about the same amount, 8.6%, higher than MOC in Sec. V.A. We conclude that most of the difference between MAGEE and experiment is due to the coarse MAGEE mesh and that a finer mesh calculation would give much better agreement.

#### ACKNOWLEDGMENTS

Most of the calculations used to investigate the computational parameter effects on the axial pressure bump were performed by R. H. Thompson. We thank

K. A. Meyer and J. F. Barnes for many helpful discussions, C. L. Mader of this Laboratory, E. L. Lee

of LLL, and B. D. Lambourn of the UK Atomic Weapons Research Establishment for their calculations.

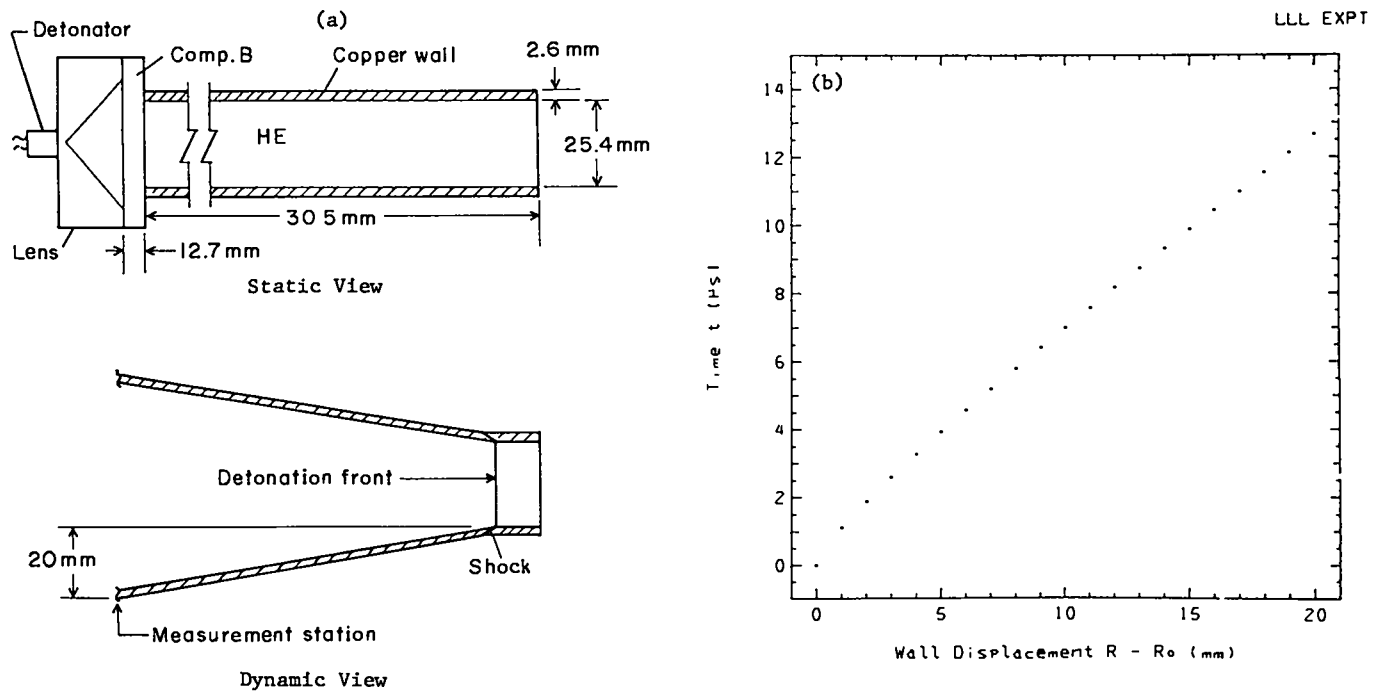


Fig. 1. Cylinder test geometry. The initiation train is SE-1 detonator, Tetryl pellet, P-22 plane-wave lens, and Composition B pad. (a) Static and dynamic views. (b) Experimental wall motion.

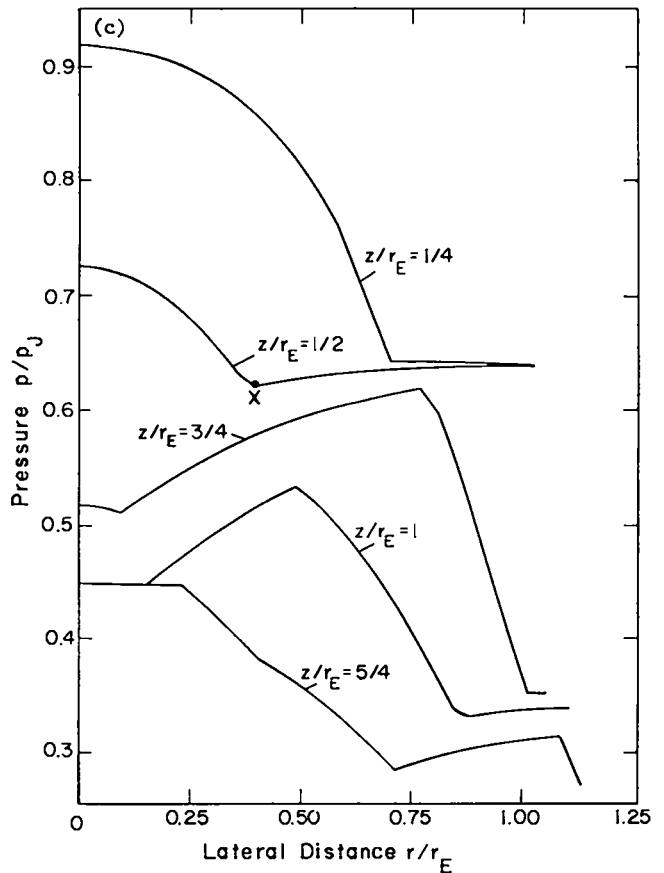
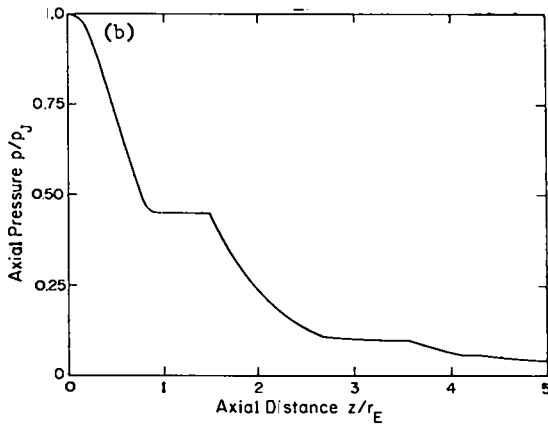
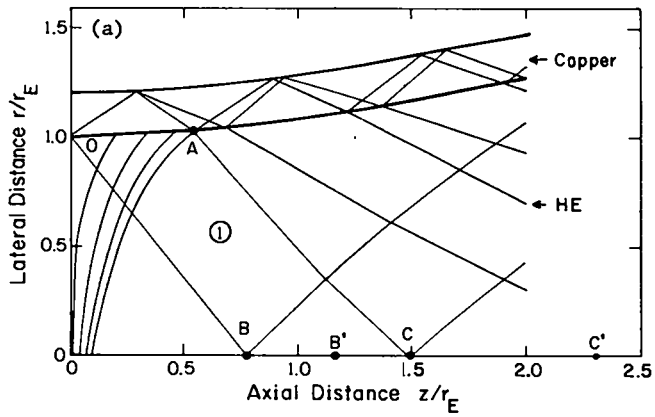


Fig. 2. Slab geometry: (a)  $r$ - $z$  diagram, (b) axial pressure vs axial distance, (c) pressure vs lateral distance. Here  $r$  is lateral distance from the symmetry plane,  $z$  is axial distance behind the front, and  $r_E$  is the half-width of the HE.

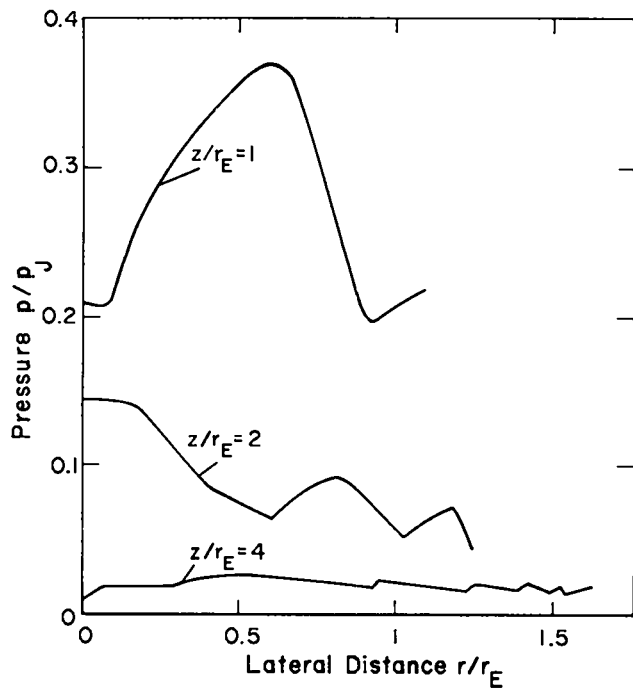


Fig. 3. Pressure vs lateral distance for the cylinder case.



Fig. 4. Flash x-ray photograph of slab geometry. The beam is centered at the intersection of the detonation front with the right wall.

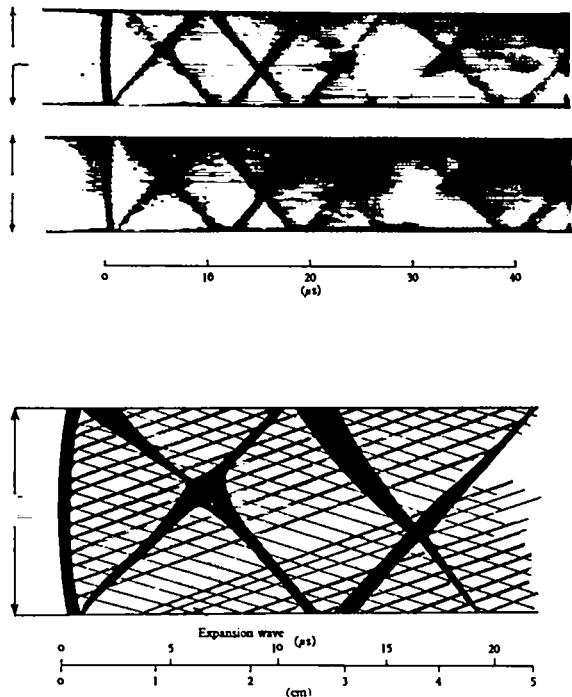
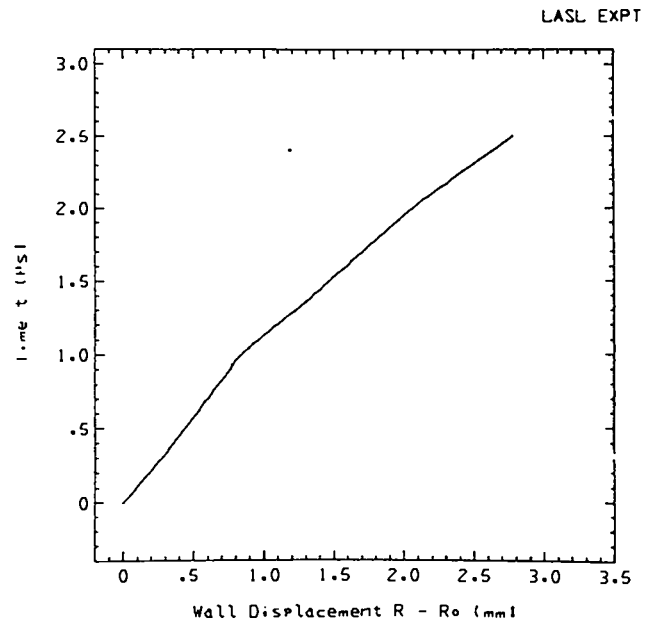


Fig. 5. Rotating-mirror camera (slit) schlieren photograph of an unsupported detonation in  $2H_2 + O_2$  at  $p_0 = 1$  atm in a 38.1-by 38.1-mm (1.5-by 1.5-in.) square cross-section tube.



AXIAL PRESSURE. MAGEE COARSE - O. MAGEE FINE - Δ. HEMP FINE - X.

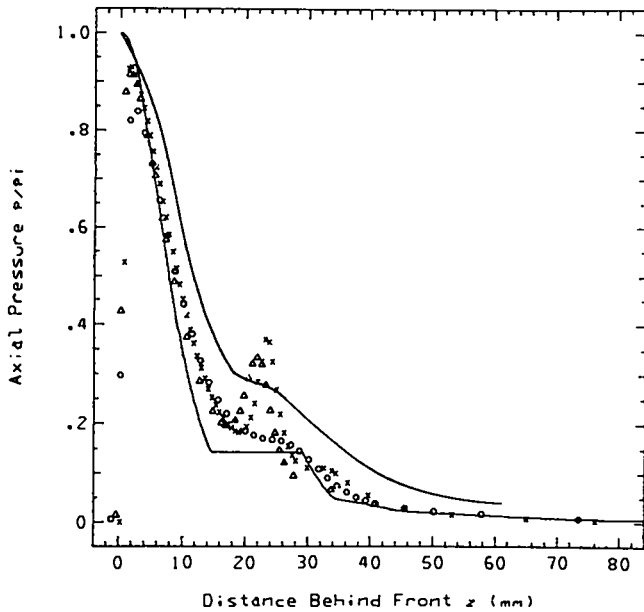


Fig. 6. Axial pressure vs distance behind the front. The lower solid line is the MOC calculation, and the upper solid line is the 2DL calculation.

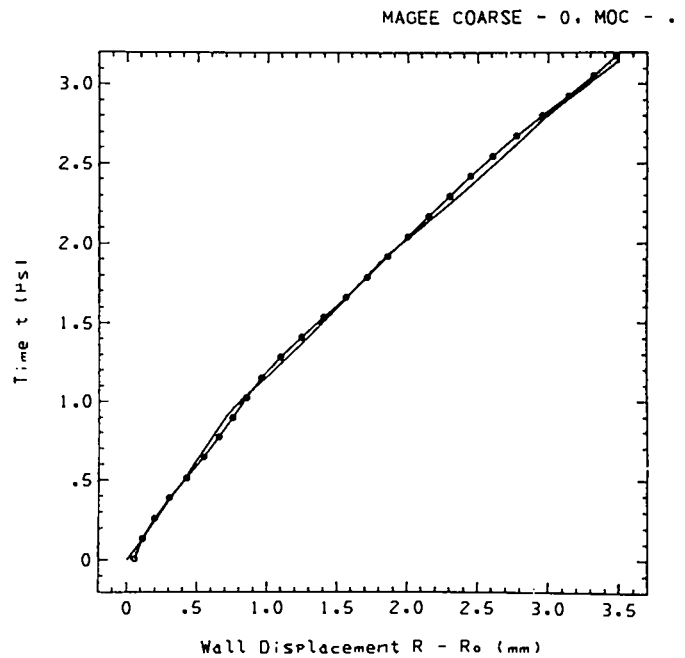
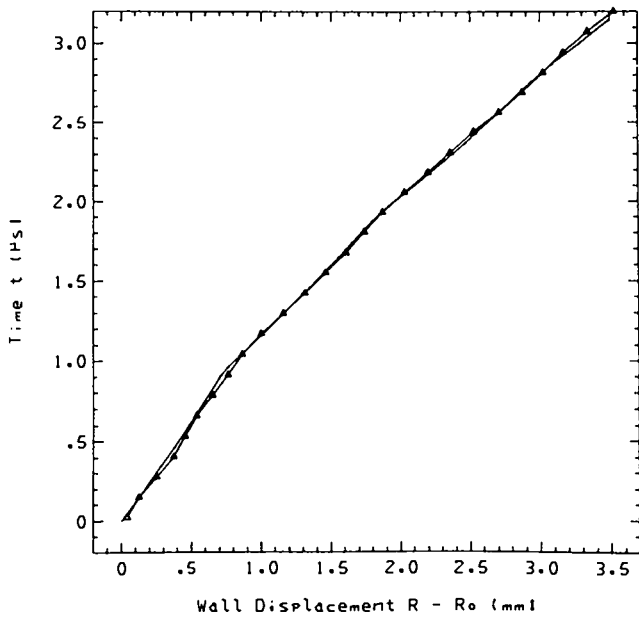
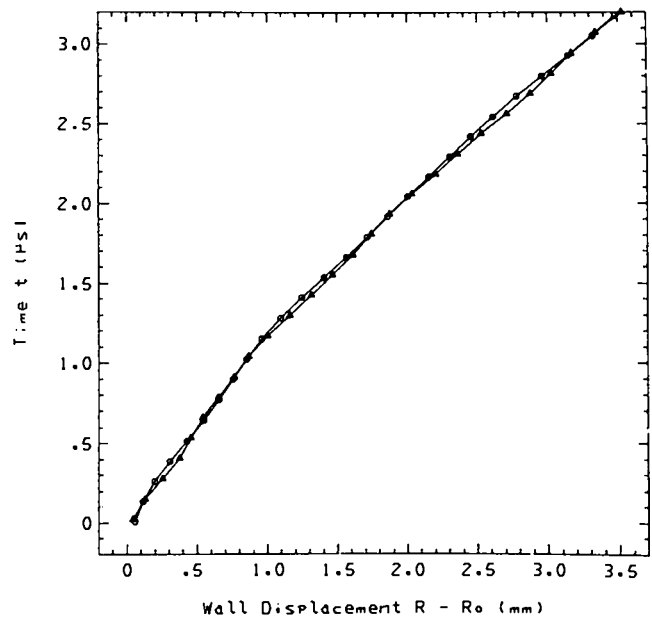


Fig. 7. Early wall motions for three mesh calculations vs MOC.

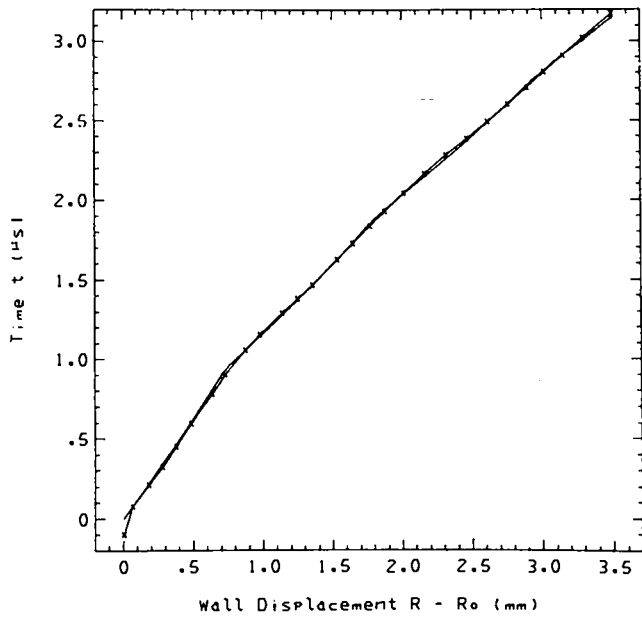
MAGEE FINE -  $\Delta$ . MOC - .



MAGEE COARSE - O. MAGEE FINE -  $\Delta$



HEMP - X. MOC - .



MAGEE COARSE - O. MAGEE FINE -  $\Delta$ . HEMP - X. MOC - .

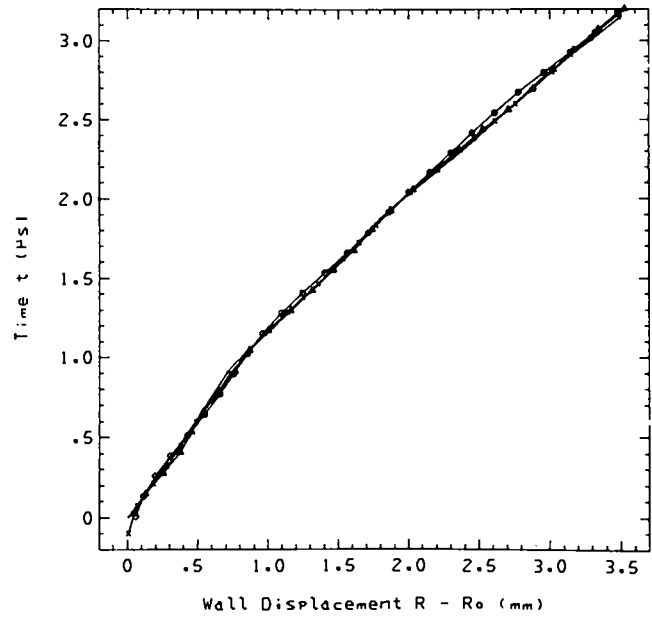


Fig. 7. Continued.

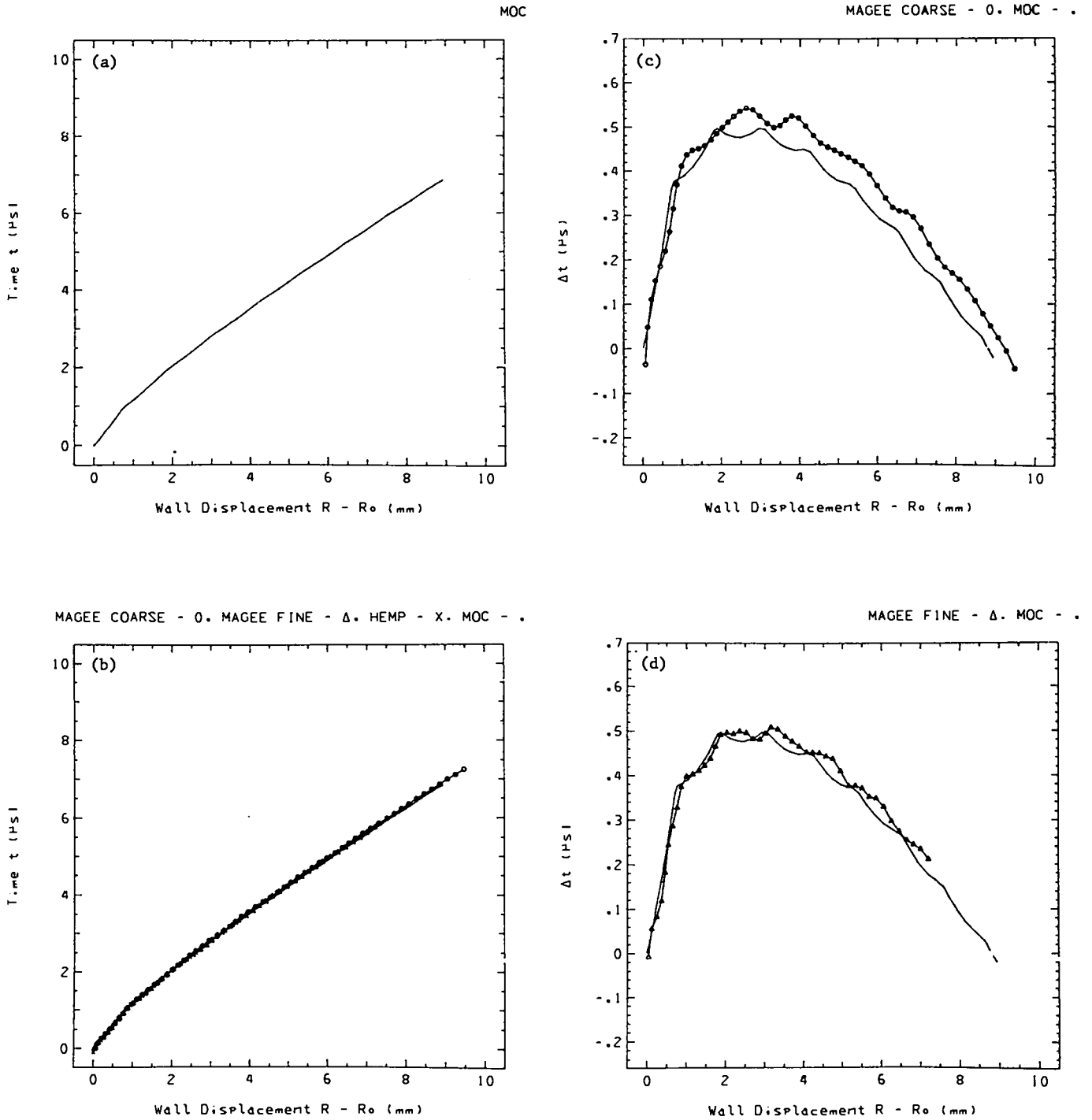
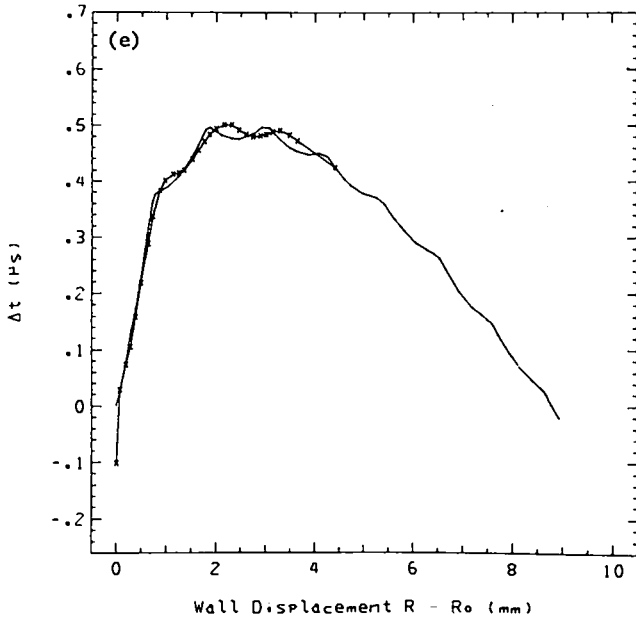
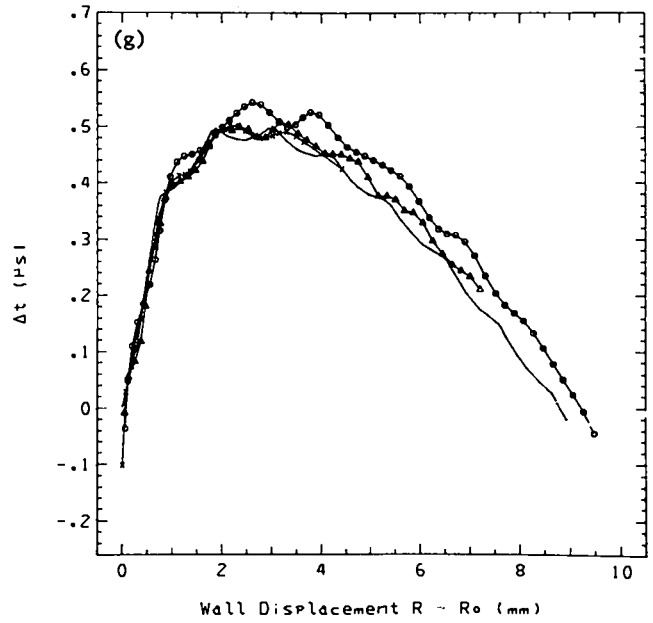


Fig. 8. Wall motions for three mesh calculations vs MOC: a and b show straight x-t plots; c-g show the differences, magnified about 14 times, by displaying time differences from a linear reference curve; and k-l show the differences, magnified about 35 times, by displaying time differences from an exponential reference curve.

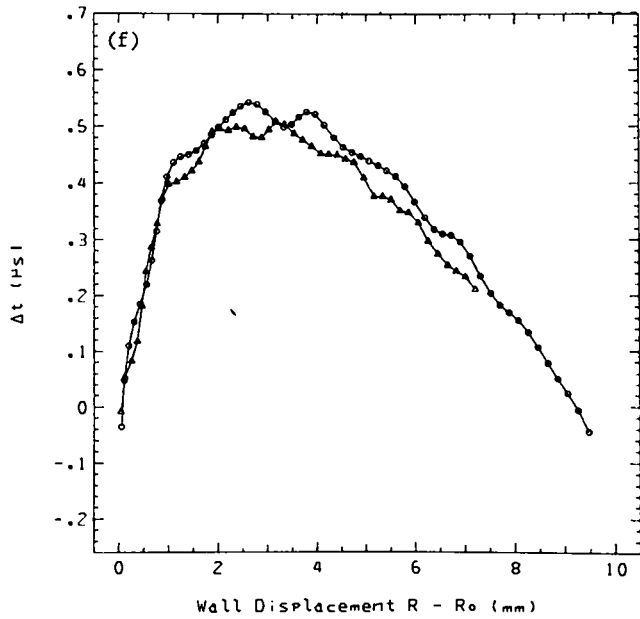
HEMP - x. MOC - .



MAGEE COARSE - 0. MAGEE FINE - Δ. HEMP - x. MOC - .



MAGEE COARSE - 0. MAGEE FINE - Δ



MAGEE COARSE - 0. MOC - .

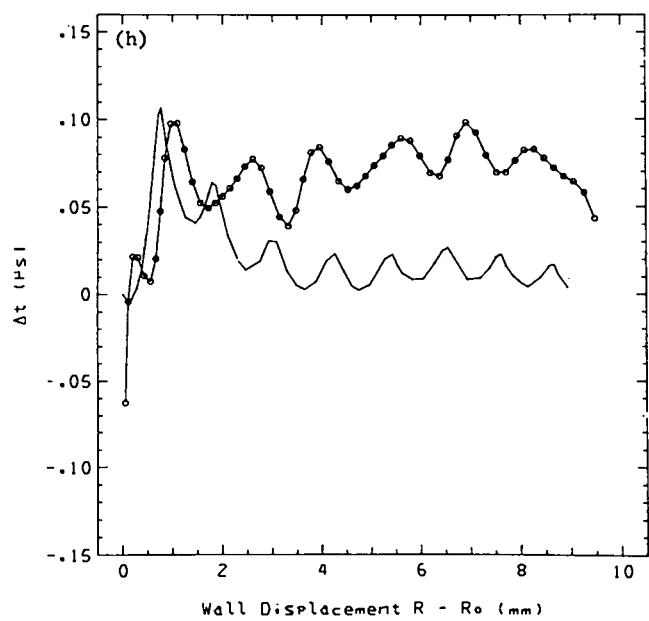
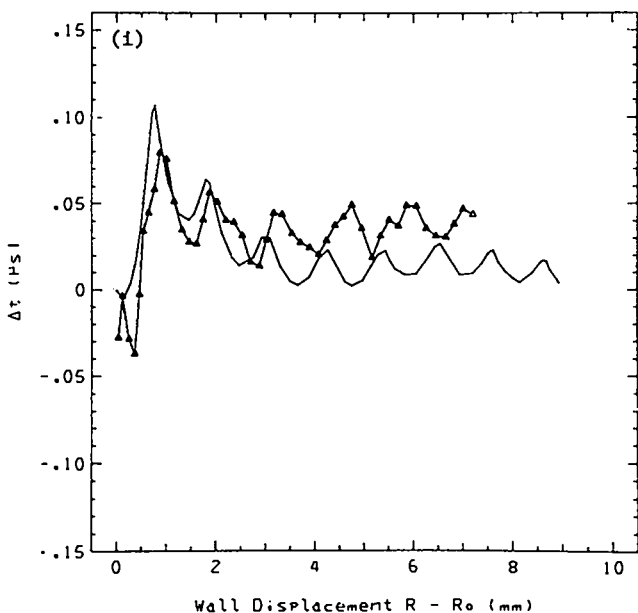


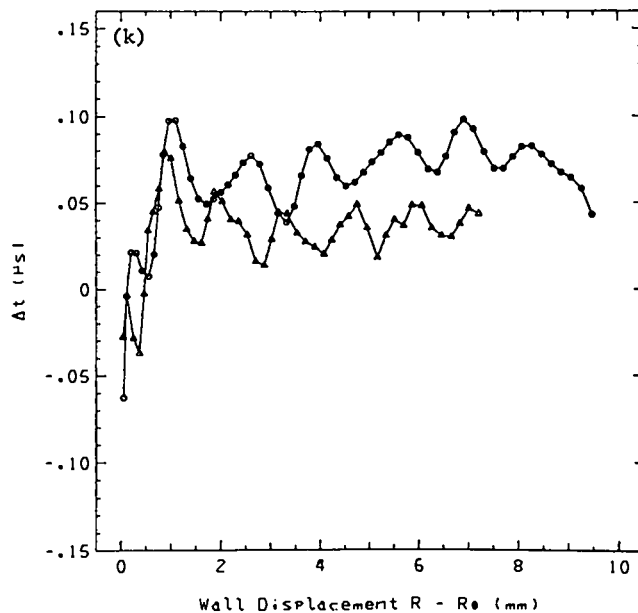
Fig. 8. Continued.



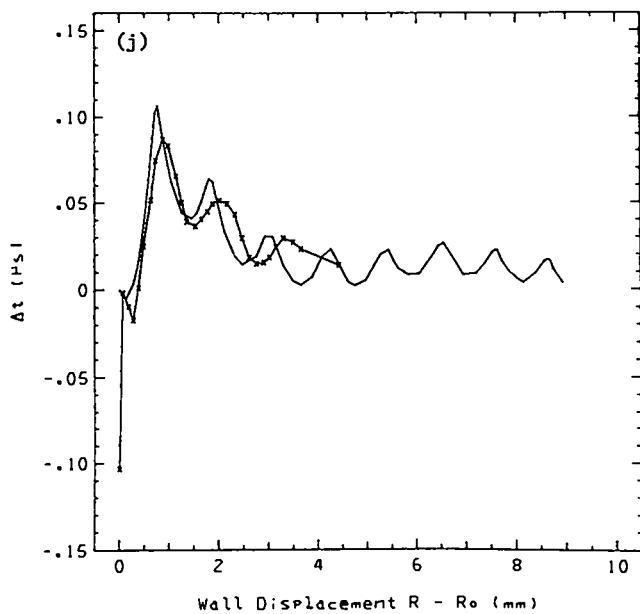
MAGEE FINE - Δ. MOC - .



MAGEE COARSE - O. MAGEE FINE - Δ



HEMP - x. MOC - .



MAGEE COARSE - O. MAGEE FINE - Δ. HEMP - x. MOC - .

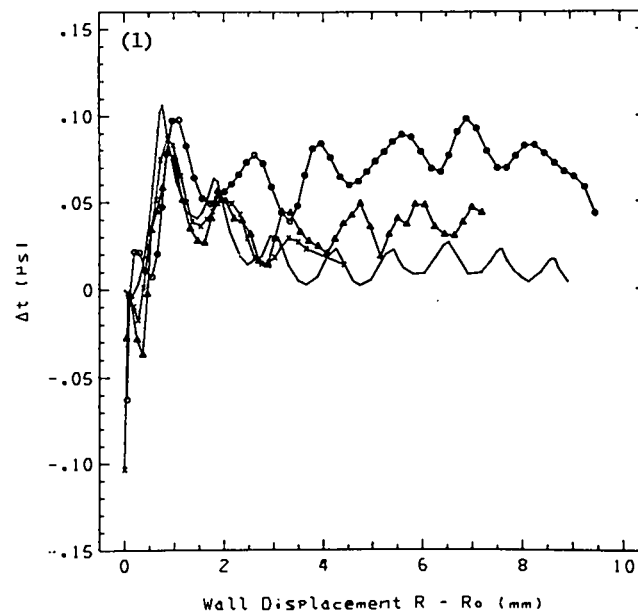
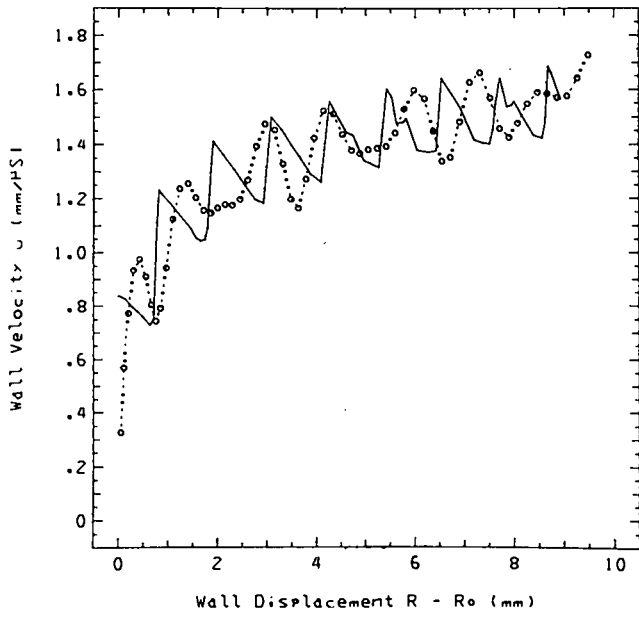
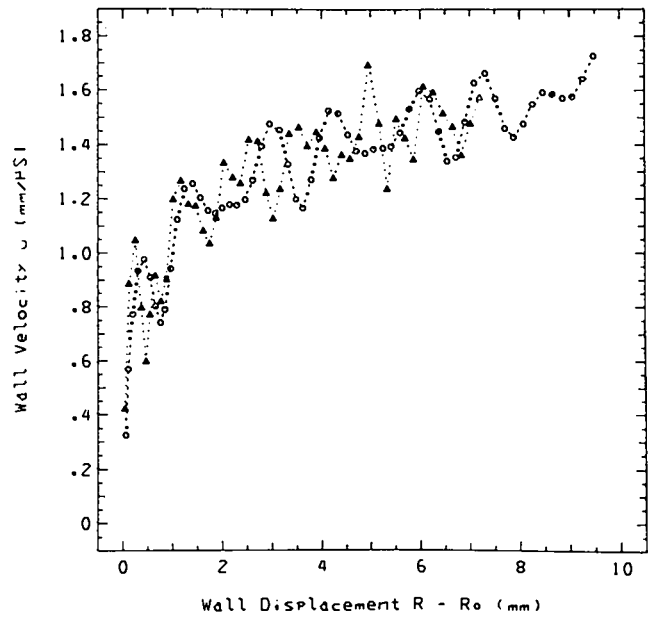


Fig. 8. Continued.

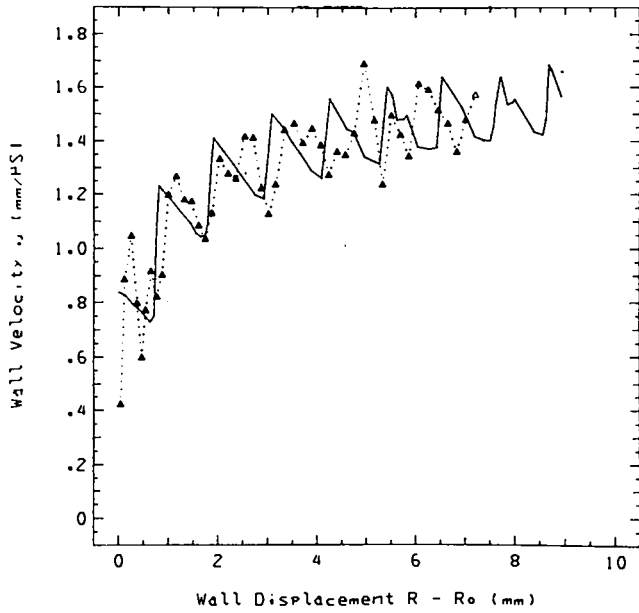
MAGEE CDARSE - 0. MDC - .



MAGEE CDARSE - 0. MAGEE FINE -  $\Delta$



MAGEE FINE -  $\Delta$ . MOC - .



MAGEE COARSE - 0. MAGEE FINE -  $\Delta$ . MOC - .

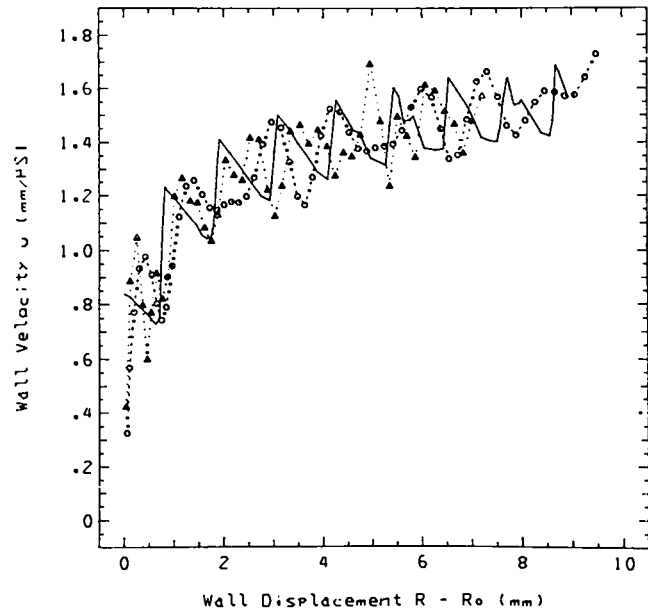


Fig. 9. Wall velocities calculated by MAGEE and MOC.

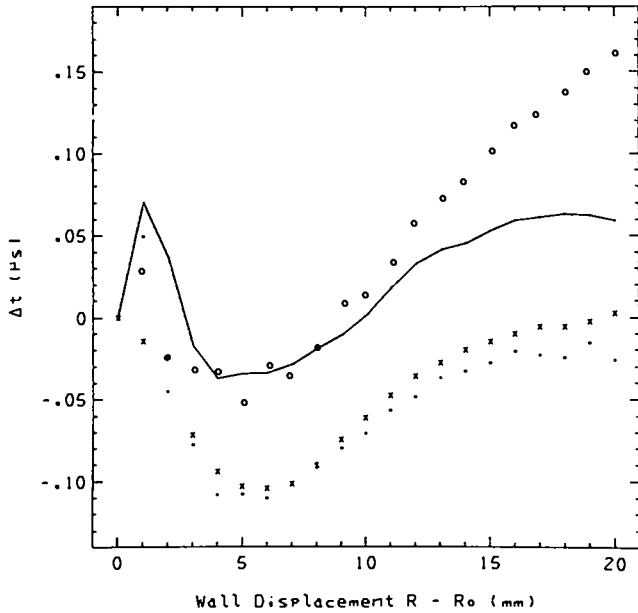


Fig. 10. Nominally identical MAGEE and HEMP calculations and LASL and LLL experiments. The solid line is the LASL experiment. The differences are magnified by displaying time differences from an exponential reference curve.

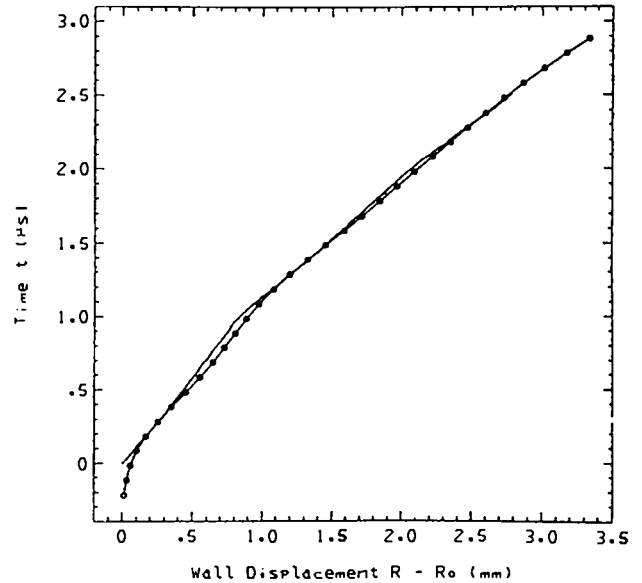


Fig. 11. Early wall motion from the LASL experiment and MAGEE calculation of Fig. 10.

## APPENDIX A

### THE MAGEE CODE

Here we briefly describe the main features of the two-dimensional Lagrangian computer code MAGEE.

#### Difference Equations

The equations for advancing the node positions and computing the cell volume from the node positions are the standard ones.<sup>10,12</sup> There are several different equations available for computing the accelerations from the stresses. Herrmann<sup>13</sup> described many of these and evaluated their performance on a selected set of prescribed distortions of the material. MAGEE uses the "force gradient" equations, with the first of the two alternative ways of approximating the denominators given by Herrmann. HEMP<sup>5</sup> uses the "Green's transformation" equations. The energy advance is also very similar in the different codes and is based on simple analogs of

#### Slip

MAGEE has the option of slip or no-slip at a material interface, i.e., letting the two materials slide freely past one another, or, in effect, gluing them together so that there is no relative motion. The method used is similar to that described in Ref. 5. In our calculation, the copper moves forward faster than the HE near the front, and vice versa to the rear. In the no-slip case, a numerical boundary layer of one-cell width develops on either side of the interface to allow slip to occur in the rest of the material. In a fluid, such as in the HE detonation products, there is no resistance to this shearing deformation of the cells. The sample output in Appendix C includes results with and without slip.

$$\dot{\epsilon} = p \dot{v} \quad .$$

### Material Strength

The model used, which is described in Ref. 14, is usually referred to as the linearly elastic, perfectly plastic, or Hooke's law-von Mises model. Linearly elastic refers to the stress and strain deviators, and not to the hydrostat, which retains its usual nonlinearity. The yield surface is a circle in a stress-deviator space with perfectly plastic flow (e.g., no work hardening) after yield.

### HE "Burn"

The HE is "burned," that is, the detonation is initiated and propagated by a chemical reaction that proceeds at a constant rate and is initiated on a surface that moves away from the initiating surface at constant velocity  $D$ . (In complicated geometries, the calculation of the initiating surface may require a Huyghens construction; here the initiating surface is a plane.)

The equation of state as given consists of a function  $\hat{p}(\rho, e)$  or  $\hat{e}(p, \rho)$  describing the detonation products, together with a value of  $e_0$  for the unreacted explosive that yields the desired CJ state when substituted into the Hugoniot and Chapman-Jouguet relations

$$\hat{e}(p, \rho) - e_0 = \frac{1}{2} p(v_0 - v)$$

$$\rho^2 c^2(p, \rho) = p/(v_0 - v) \quad ,$$

where  $c$  is sound speed,

$$\rho^2 c^2(p, \rho) = (p + \hat{e}_v)/\hat{e}_p \quad ,$$

with the subscripts  $p$  and  $v$  denoting partial differentiation. Our burn method requires a "complete" equation of state  $\tilde{p}(\rho, e, \lambda)$  which describes the mixture of reacted and unreacted explosive. For the complete equation of state we choose the simple form

$$\tilde{p}(\rho, e, \lambda) = \hat{p}[\rho, e - e^* + \lambda(Q + e^*)] \quad ,$$

with the heat of reaction  $Q$  numerically equal to the given  $e_0$ , and the value of  $e^*$  chosen to make the calculated initial pressure of the unreacted explosive,  $\tilde{p}(\rho_0, e_0, \lambda = 0)$ , equal to zero for whatever

value of  $e_0$  we decide to use in the MAGEE calculation (we take  $e_0 = 0$  for this purpose). As an example, take a  $\gamma$ -law for  $\hat{p}(\rho, e)$

$$\hat{p}(\rho, e) = (\gamma - 1)\rho e \quad .$$

The complete form is

$$\tilde{p}(\rho, e, \lambda) = (\gamma - 1) \rho(e + \lambda Q) \quad ,$$

with  $e^* = 0$ .

The progress of the reaction is described by a reaction rate  $r$

$$\dot{\lambda} = r = \hat{r}(\rho, e, \lambda) \quad .$$

The energy advance equation is unchanged by the presence of reaction, being (for a fluid)

$$\dot{e} = p \dot{v} \quad .$$

A constant reaction rate

$$r = \tau^{-1}; \quad \tau = k \Delta z_0 / D$$

is used with reaction time  $\tau$ , depending on the initial cell thickness  $\Delta z_0$ , the constant detonation velocity  $D$ , and a constant multiplier  $k$ , which is normally one. Reaction starts in cell  $i$  at an ignition time  $t_i$

$$t_i = z_i / D - \frac{1}{2} \tau \quad ,$$

where  $z_i$  is the distance of the center of cell  $i$  from the initiating plane. Thus, the value of  $\lambda$  in cell  $i$  is a function of time alone.

$$\lambda = 0 \text{ for } t < t_i \quad ,$$

$$\lambda = t - t_i \text{ for } t_i \leq t \leq t_i + \tau \quad ,$$

and

$$\lambda = 1 \text{ for } t > t_i + \tau \quad .$$

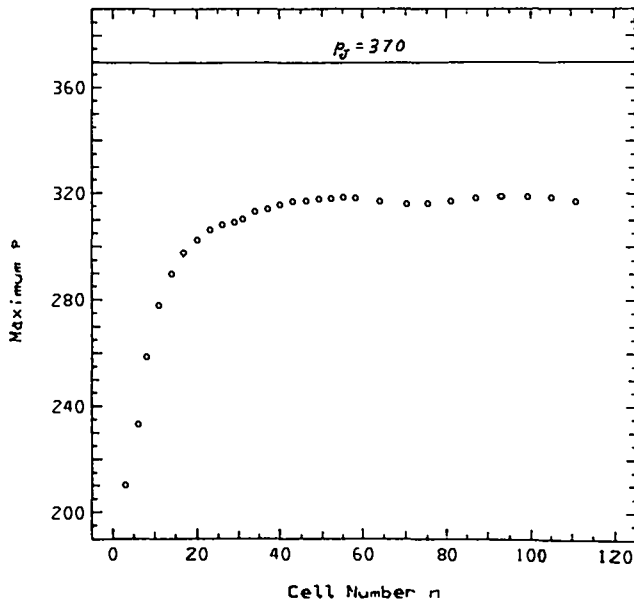


Fig. A-1. Initiation of detonation: front (maximum) pressure vs cell number. Cell 50 is at a distance of 75 mm, or 3 HE diameters, from the initiating plane.

The cell at the initiating plane is treated like the others. Note that for that cell,  $t_1 = t_0$ , so that it begins to react immediately.

In our calculation, the peak pressure at the wave front increases with distance of run. In a typical case (our coarse mesh), the peak pressure is very nearly a hyperbolic function of distance. Using the cell number  $n$  of the peak-pressure cell in place of distance, this relation is

$$p - p^* = -k/(n - 3) \quad ,$$

$$p^* = 0.86 p_j, \quad k = 28.3 \text{ GPa} \quad .$$

The peak pressures are shown in Fig. A-1. They oscillate slightly after reaching their highest point at cell 55.

#### Time Step

The time step is set from a stability condition that is based on an approximate linearized stability analysis, plus a safety factor. Without artificial

viscosity, one could use a value close to the Courant condition  $\Delta t = \Delta z/c$ , where  $\Delta z$  is the length of the smaller side of the cell and  $c$  is the sound speed. With artificial viscosity, the complete stability condition gives values of about one-third or one-fourth the Courant value; experience confirms that such a value works well. Values observed in actual runs in this work are about one-eighth the Courant value and sometimes appreciably smaller when the cells in the rear become distorted.

#### Artificial Viscosity

The standard artificial viscosity is the von Neumann-Richtmeyer quadratic form

$$q = B \rho A (v/v)^2; \quad v \equiv 1/\rho$$

$$\dot{v}/v = (v^{n+1} - v^n)/(v^{n+1} \Delta t) \quad .$$

$$B = 1.44 \quad ,$$

where the index  $n$  denotes the time step and  $A$  the cell area. Other forms are also available.

#### Cell Distortion

The main problem with programs of this type is computation-cell distortion. The offending cells are those near the intersection of the rear boundary with the copper/HE interface. Ordinarily, these cells become sufficiently distorted to stop the calculation; the stop is postponed, but not eliminated, by an ad hoc automatic cell-resaping mechanism built into the program. Allowing slip aggravates the problem. Giving the copper some elastic strength stiffens it enough to reduce the cell distortion greatly, thereby allowing the slip option to be used.

In the calculations used to compare with MOC, which used fluid copper, cell distortion was a serious problem. The calculation could be run for a longer time by periodically removing a rear section of the net and applying a continuative boundary condition to the freshly exposed surface, but even so we were unable to carry the calculation as far as we would have liked.

APPENDIX B

DISPLAY

Reference Curve

In presenting some of the wall motion results, we use time differences from smooth reference curves for greater magnification. The exponential reference curve is based on a simple exponential function for  $u(x)$

$$u = u_0 + (u_\infty - u_0) \left(1 - e^{-x/\hat{x}}\right)$$

with parameters  $u_0$ ,  $u_\infty$ , and  $\hat{x}$ . This integrates to

$$t = u_\infty^{-1} \left( x + \hat{x} \log \left\{ u_0^{-1} \left[ u_\infty - (u_\infty - u_0) e^{-x/\hat{x}} \right] \right\} \right) .$$

In presenting  $t-x$  results, we must determine  $t_0$ , the time at which the wall begins to move. This is poorly determined in a mesh calculation because of the gradual initial acceleration due to artificial viscosity and finite cell size. Extrapolation from an early segment of the curve is unsatisfactory because the velocity is rapidly changing. For all of our calculations, we arbitrarily picked  $t_0$  to match the MOC time at 1.88 mm of wall displacement in Sec. V.A and the LLL experiment time at 2 mm in Sec. V.B. For the HEMP calculations,<sup>1,3</sup> we used the  $t_0$  values as reported.

Eulerian from Lagrangian Velocities

MAGEE calculates Lagrangian (particle) velocities. We need the Eulerian radial velocity at a fixed  $z$ , that is,  $(\partial R/\partial t)_z$ . These velocities are

related by

$$(\partial R/\partial t)_z = (\partial R/\partial t)_h - (\partial R/\partial z)_t (\partial z/\partial t)_h ,$$

where subscript  $h$  denotes a Lagrangian (constant particle) derivative. The Lagrangian radial and longitudinal velocities on the right side are printed out by the code. The wall slope at fixed time,  $(\partial R/\partial z)_t$ , was estimated by difference. The second term on the right side fluctuates somewhat but is relatively small, typically 1.5% of the first term.

Data Collection

The MAGEE data for comparison with MOC (Sec. V.A) were collected by a patch to MAGEE, which at specified times interpolated wall positions and velocities to a set of specified values of  $z$ . Using this patch has a very slight effect on the results, inasmuch as MAGEE shortens each time step that would bracket a specified time so as to land right on the specified time. In Sec. V.B, the data were read from the printout at a given time. Once steady flow is attained, the one set of data are of course related to the other set by

$$R = R; z_f - z = Dt ,$$

where  $z_f$  is the front position. The use of the patch is convenient in checking for steadiness because the results are obtained at given  $z$ .

APPENDIX C

MOC CALCULATION SPECIFICATIONS AND DETAILS

The MOC calculation is described in Ref. 4, and some of its assumptions are discussed in Sec. III.

The HE is

$$\text{LX-04-01, } \rho_0 = 1.865 \text{ Mb/m}^3$$

$$D = 8.48 \text{ mm}/\mu\text{s}, \gamma = 2.726, p = 35.994 \text{ GPa},$$

represented by the Wilkins equation of state<sup>15</sup>

$$p = a V^b + B(1 - w/RV)e^{-RV} + wE/V$$

$$V \equiv v/v_0$$

$$E \equiv \rho_0 [e - e^* + \lambda(Q + e^*)]$$

$$a = -0.08335 \text{ GPa}$$

$$b = -4$$

$$B = 594.3 \text{ GPa}$$

$$R = 4$$

$$w = 0.4$$

$$\rho_0 Q = 11.26 \text{ GPa}$$

$$\rho_0 e^* = 24.2828$$

We give the complete form of the equation of state described in Appendix A since it is also used in a MAGEE calculation (the MOC calculation needs the equation of state only for  $\lambda = 1$ ). The (fluid) copper is represented by the equation of state

$$p = 140.7 \mu + 287.1 \mu^2 + 233.5 \mu^3$$

$$\mu \equiv \rho/\rho_0 - 1, \rho_0 = 8.90$$

The original calculation has a unit HE radius and a

wall thickness of 0.203. For an HE radius of 12.7 mm, the corresponding wall thickness is 2.5781 mm, which is slightly less than our standard of 2.6 mm.

The standard coarse mesh (10 + 3) for the MAGEE calculations is

$$300 \text{ longitudinal cells: } \Delta z = 1.5 \text{ mm}$$

$$10 + 3 \text{ lateral cells: } \Delta r = 1.27 \text{ mm (HE)}$$

$$\Delta r = 0.866 \dots \text{ mm (copper)}.$$

The fine mesh (20 + 6) has all cell dimensions reduced by a factor of 2. Unless otherwise stated, all MAGEE calculations used the standard parameters described in Appendix A, a continuative rear boundary condition, and the dimensions listed in Table I.

In Sec. V.A (compare with MOC), the MAGEE calculation uses the same equations of state and dimensions as MOC, thus no material strength for copper, and no slip.

In Sec. V.B, all calculations are for the HE

$$\text{PBX 9404, } \rho_0 = 1.84 \text{ Mg/m}^3$$

$$D = 8.8 \text{ mm}/\mu\text{s}, \gamma = 2.85, p = 37.0 \text{ GPa},$$

represented by the JWL equation of state<sup>7</sup>

$$p = A \left(1 - \frac{\omega}{R_1 V}\right) e^{-R_1 V} + B \left(1 - \frac{\omega}{R_2 V}\right) e^{-R_2 V} + \frac{\omega E}{V}$$

$$V = v/v_0$$

$$E = \rho_0 [e - e^* + \lambda(Q + e^*)]$$

$$A = 854.45 \text{ GPa}$$

$$B = 20.493 \text{ GPa}$$

$$\omega = 0.25$$

$$R_1 = 4.6$$

$$R_2 = 1.35$$

$$\rho_o Q = 10.2 \text{ GPa}$$

$$\rho_o e^* = 49.8051 \text{ GPa}$$

For copper, we used the standard MAGEE equation of state for the hydrostat

$$p = (a + bE + cE^2)/(E + E_c)$$

$$a = a_o \mu + a_1 \mu |\mu|$$

$$b = b_o + b_1 \mu + b_2 \mu^2$$

$$c = c_o + c_1 \mu$$

$$\mu = \rho/\rho_o - 1$$

$$E = \rho_o e$$

$$\rho_o = 8.93$$

$$a_o = -4.9578323 \times 10^4 \text{ (GPa)}^2$$

$$a_1 = 3.6883726 \times 10^4 \text{ (GPa)}^2$$

$$b_o = 747.27361 \text{ GPa}$$

$$b_1 = 1151.9148 \text{ GPa}$$

$$b_2 = 5525.1138 \text{ GPa}$$

$$c_o = 3.9492613 \times 10^{-3} \text{ (GPa)}^{-1}$$

$$c_1 = 5.2883412 \times 10^{-3} \text{ (GPa)}^{-1}$$

$$E_c = 360 \text{ GPa}$$

For the material strength constants, all calculations used  $Y_o = 0.3 \text{ GPa}$  for the yield strength and a standard value of  $47.7 \text{ GPa}$  for the Lamé constant  $\mu$ . Slip was allowed at the HE/copper interface.

Selected snapshots for the above-described MAGEE calculations are shown in Fig. C-1 and input data are given in Tables C-I through C-III.



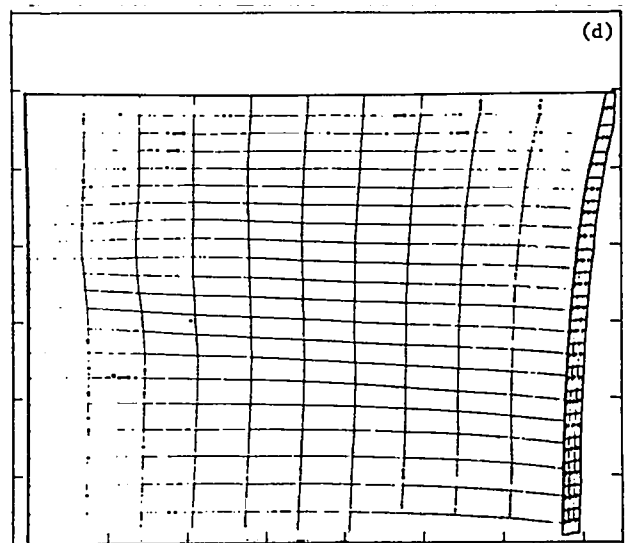
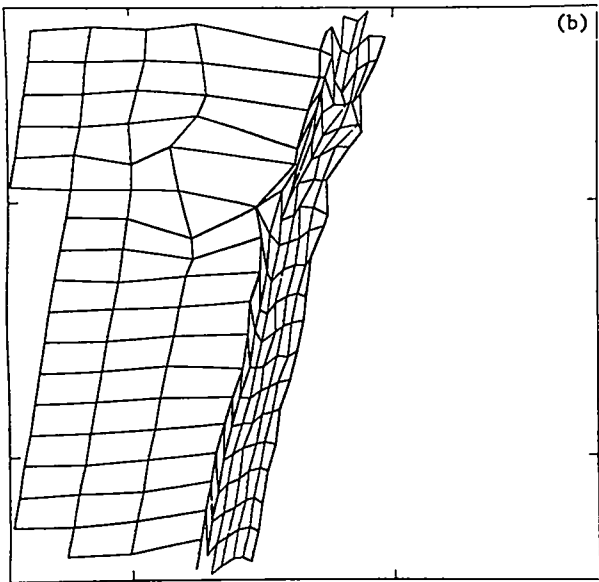
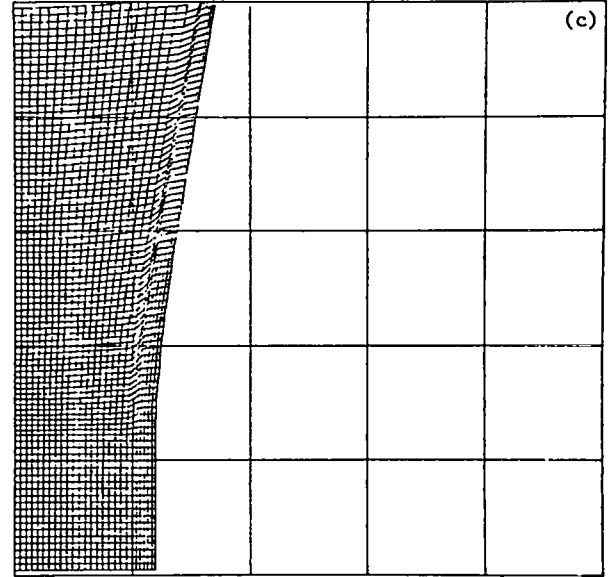
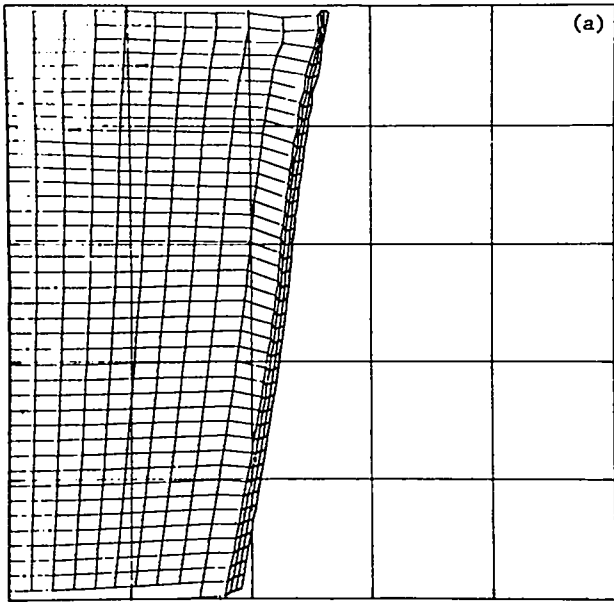


Fig. C-1. Snapshots from MAGEE calculations. The detonation runs downward. (a) Coarse mesh, Sec. V.A,  $t = 11.7$ , initiation end. (b) Fine mesh, Sec. V.A,  $t = 15.1$ , rear end computation net after removal of zones in rear. (c) Fine mesh, Sec. V.A,  $t = 15.1$ , near detonation front. (d) Coarse mesh, Sec. V.B,  $t = 17.5$ , initiation end.

TABLE C-I

COARSE MAGEE, SEC. V.A, INPUT

```

ACC
PSSU      TITLE=5GM      EG6-01-13VV      06/23/75
TDUMF= 0.5.
      ENDTIM=40.
IGAC=6.6.6.3.1.2.3.2.2.
RAI-G=0.0.0.90.0.90.0.0.
      AREAPO6=.T..
PLANE=.F.. SVELLIP=.F.. SURECT=.T.. SUBURN=.T.. JRAOIAL=.F..
      ND-BURN=.T..
TFIN=0..1.
PINDATA=22.20.18.16.
TUNZCHE=12.5.17.2.19.3.22.2.24.99.
      FUDGCLD=2.
      JSFACE=10.3. ISPACE=300.
      DELTAJ=.1. .0676666. DELTAI=-.11811.
STARTJ=0.0. STARTI=30.48. ILAST=301. JLAST=14.
TFILM=0..5.TIPRINT=100.10.
      M1=140.300.
      ESN=140.12.1.865.-10.0.0..35553..648.
      ESN(1,2)=300.15.8.9.-1E10. 160..59.
      TCPLCT=0..5. 6..5. 10.5..5. 16..5. 21..5. 26..5.
      TVPLOT=0..3. 6..5. 10.3..3. 16..3. 21..5. 26..5.
      FILMCM=0.10.0.1.1. 0.30.5.0.1.1.
      0.5.0.1.1. 25.5.30.5.23.5.1.1.
      0.5.0.1.1. 20.5.25.5.20.5.1.1.
      0.5.0.1.1. 16.5.21.5.16.5.1.1.
      0.5.0.1.1. 12.0.17.0.12.0.1.1.
      0.5.0.1.1. 7.5.12.5.07.5.1.1.
      0.5.0.1.1. 3.0.08.0.03.0.1.1.
      KVPLOT(1,1)=6=1.
      KVPLOT(1,2)=0.3=2.
      KVPLOT(1,3)=2.3.4.5.6.7.
      KCPLOT(1,1)=2.3.4.5.6.7.
      KCPLOT(1,2)=0.2.3.4.5.6.
      CCONT=5=0. .1..1..4.3.0. .1..1..4.3.0. .1..1..4.3.0.
      .1..1..4.3.0. .1..1..4.3.0. .1..1..4.3.0.
      SENDSU
P8BURN IRAO=300.ZLINE=30.48.0.10.
      IBA PCJ=2.
      VBIT=1.0.0.
      SENDBURN
P8UNZONE IRZ=1GSHAVEI . RZLIM=17.301. 8
P8UNZONE 8
P8UNZONE IRZ=1GSHAVEI . RZLIM=34.301. 8
P8UNZONE 8
P8UNZONE IRZ=1GSHAVEI . RZLIM=51.301. 8
P8UNZONE 8
P8UNZONE IRZ=1GSHAVEI . RZLIM=68.301. 8
P8UNZONE 8
P8UNZONE IRZ=1GSHAVEI . RZLIM=85.301. 8
P8UNZONE 8
P8SU 8

```

\*\*\*\*\* THE FOLLOWING CARDS WERE ADDED BY MAGEE \*\*\*\*\*  
P8BJAN SUSCD ONLY IN THE ABSENCE OF OTHER BURN CARDS. (ADDED BY MAGEE)

TABLE C-II

FINE MAGEE, SEC. V.A, INPUT

```

ACD
PSSU      TITLE=30H      E06-01-112V      08/23/75
TCUHP= 0.5,
          ENDTIM=40,
IGRAD=6.6.6.3.1.2.3.2.2,
RANG=0.0.0.90.0.90.90.0.0,
          AREAF06=.T..
PLANE=.F.. SUELLIP=.F.. SURECT=.T.. SUBURN=.T.. JRADIAL=.F..
          NEWBURN=.T..
TPIN=.0.1.
PINDATA=22.20.18.16,
TUNONE=12.5.17.2.19.3.22.2.24.99,
          FUDGE=2,
          JSPACE=20.6, ISPACE=300,
          DELTAJ=.05, .0336333, DELTAI=-.059055,
STARTJ=0.0, STARTI=30.48, ILAST=301, JLAST=27,
TFILM=0.5, TPRINT=100,10,
          M1=140,300,
          ESN=140.12.1.065.-10.0.0.35533,.848,
          ESN(1,2)=300.15.8.9.-1E10. 1600.39,
          TCPL0T=0.5. 6.5. 10.5.5. 16.5. 21.5. 26.5,
          TVPLOT=0.5. 6.5. 10.5.5. 16.5. 21.5. 26.5,
          FILMDH=0.10.0.1.1. 0.30.5.0.1.1,
                   0.5.0.1.1. 25.5.30.5.25.5.1.1,
                   0.5.0.1.1. 20.5.25.5.20.5.1.1,
                   0.5.0.1.1. 16.5.21.5.16.5.1.1,
                   0.5.0.1.1. 12.0.17.0.12.0.1.1,
                   0.5.0.1.1. 7.5.12.5.07.5.1.1,
                   0.5.0.1.1. 3.0.08.0.03.0.1.1,
          KVPLOT(1,1)=0*1,
          KVPLOT(1,2)=0,5*2,
          KVPLOT(1,3)=2,3,4,5,6,7,
          KCPLC(1,1)=E.3.4.7.C.7,
          KCPLC(1,2)=0.2.3.4.3.6,
          CCONT=9*0, .1.1.1.4.3.0, .1.1.1.4.3.0, .1.1.1.4.3.0,
                   .1.1.1.4.3.0, .1.1.1.4.3.0, .1.1.1.4.3.0,
$ENDSU
PSBURN  IRAD=300.ZLINE=30.48.0.20,
          IDRPCJ=2,
          VBIT=1.0.0,
$ENDBURN
PSUNZONE IRZ=10HSHAVEI . RZLIM=34.301. 8
PSUNZONE S
PSUNZONE IRZ=10HSHAVEI . RZLIM=68.301. 8
PSUNZONE S
PSUNZONE IRZ=10HSHAVEI . RZLIM=102.301. 8
PSUNZONE S
PSUNZONE IRZ=10HSHAVEI . RZLIM=136.301. 8
PSUNZONE S
PSUNZONE IRZ=10HSHAVEI . RZLIM=170.301. 8
PSUNZONE S
PSSU S

```

\*\*\*\*\* THE FOLLOWING CARDS WERE ADDED BY MAGEE \*\*\*\*\*  
 PSBURN SUSCD ONLY IN THE ABSENCE OF OTHER BURN CARDS. (ADDED BY MAGEE)

TABLE C-III

(COARSE) MAGEE, SEC. V.B, INPUT

```

NOMAG
PSSU TITLE=50H E06-01-11V11 04/08/73
TDUMP= 0.5.
ICRAD=3.3.3.3.1.2.3.2.2. ENDTIM=40.
RANG=0.0.0.90.0.00.90.0.0.
      AREAPOS=.T..
PLANE=.F.. SUELLIP=.F.. SURECT=.T.. SUBURN=.T.. JRADIAL=.F..
MI=159.331.
ESC=159.12..1.04.-1.E4.0.545..20493..59972187..88.4.60.
1.35..25..49805077.
      NEWBURN=.T..
TPIN=0..1.
PINDATA=28..18..16..14..12..10..8..6..
      JREG=2.
      ELPL=.T.. ESCV(1,1)=331.11*0..477..003.
      JSPACE=10.3. ISPACE=300.
      DELTAJ=-.127. .086666666. DELTAI= -.15.
STARTJ=0.0. STARTI=30.48. ILAST=301. JLAST=14.
TFILM=0..5.TIPRINT=100.10.
TCPLOT=0..5.3..5.6..5.9..5.
TPPLOT=0..5.3..5.6..5.9..5.
TVPLOT=0..5.3..5.6..5.9..5.
FILMDM=0.25.0.5.5.15.40.0.5.5.1.4.1.3.3.29.32.29.3.3.
1.4.1.3.3.27.29.27.3.3.1.4.1.3.3.24.27.24.3.3.1.4.1.3.3.21.24.21.3.3.
KPLOT(1,1)=1.1.1.1.
KPLOT(1,2)=2.3.4.5.
KCPLT(1,1)=1.1.1.1.
KCPLT(1,2)=2.3.4.5.
KVPLT(1,1)=1.1.1.1.
KVPLT(1,2)=2.3.4.5.
CCONT=.1..1..4.3.0. .1..1..4.3.0. .1..1..4.3.0. .1..1..4.3.0.
      .1..1..4.3.0.
SENDSU
PSBURN IRAD=300.ZLINE=30.48.0.10.
      IBRPCJ=2.
      VBIT=1.0.0.
SENBURN
PSSU $

```

..... THE FOLLOWING CARDS WERE ADDED BY MAGEE \*M\*\*\*\*M\*\*\*\*\*  
 PSBURN USED ONLY IN THE ABSENCE OF OTHER BURN CARDS. (ADDED BY MAGEE)

ALTERED MATERIAL	159	12					
	.1840000000E+01	-.1000000000E+05	.8545000000E+01	.2049300000E+00	.5997218700E+00	.8800000000E+00	
	.4600000000E+01	.1350000000E+01	.2500000000E+00	.4980507700E+00	0.	0.	
	0.	0.	0.	0.	0.	0.	
	0.	0.	0.	0.	0.	0.	
	0.	0.	0.	0.	0.	0.	
ALTERED MATERIAL	32!	2					
	.8899999000E+01	-.1000000000E+02	.4957832300E+01	.3688372600E+01	.7472736100E+01	.1151914800E+02	
	.5525113800E+01	.3949261300E+00	.5288341200E+00	.3600000100E+01	.4770000000E+00	.3000000000E-02	
	0.	0.	0.	0.	0.	0.	
	0.	0.	0.	0.	0.	0.	
	0.	0.	0.	0.	0.	0.	

APPENDIX D  
DATA FOR FIGURES

These tables contain all the data presented in Figs. 6-10.

TABLE D-I  
DATA FOR FIG. 6

MAGEE COARSE P										
	6.7235E-03	.2973059	.8205709	.8398523	.7950661	.7293315	.6555399	.5808036	.5082900	.4408329
11	.3801270	.3270615	.2827198	.2481022	.2200136	.1995931	.1855904	.1770888	.1719212	.1692540
21	.1656145	.1583631	.1457496	.1285519	.1093817	.0907393	.0748474	.0618450	.0520653	.0445084
31	.0388129	.0281720	.0224487	.0169754	7.8904E-03	6.2790E-03				
MAGEE COARSE X										
	-1.1124440	.2522980	1.4354300	2.6000200	3.7798500	4.9876200	6.2246000	7.4920600	8.7900000	10.1171500
11	11.4709700	12.8501900	14.2484600	15.6632400	17.0919900	18.5309000	19.9774300	21.4277700	22.8806500	24.3360700
21	25.7927600	27.2532600	28.7201100	30.1971200	31.6830200	33.1816200	34.6878400	36.2042200	37.7269500	39.2547600
31	40.7863800	45.4015600	50.0357900	57.7586600	73.3491800	105.1131500				
MAGEE FINE P										
	.0141693	.4283305	.8772760	.9148942	.9133939	.8933624	.8639680	.7893706	.7057160	.6172549
11	.5729688	.4876194	.3739592	.2854425	.2246533	.2017601	.1962313	.1964536	.2053719	.2250701
21	.2553813	.2908880	.3207825	.3335071	.3186988	.2773855	.2264037	.1812285	.1471666	.1229676
31	.0953790	.0665959	.0373681							
MAGEE FINE X										
	-.4615500	.2013900	.7792400	1.3456600	1.9120800	2.4823100	3.0576200	4.2323700	5.4401400	6.6834700
11	7.3197400	8.6176800	10.6306300	12.7083500	14.8343300	16.2707000	16.9907900	17.7108800	18.4297000	19.1421700
21	19.8482900	20.5455200	21.2364000	21.9247400	22.6168900	23.3166600	24.0291300	24.7530300	25.4858200	26.2249600
31	27.7159400	33.7446300	40.6064400							
HEMP P										
	0	.5270265	.9259991	.9284856	.9146477	.8961613	.8723235	.8451883	.8174857	.7890533
11	.7565668	.7229182	.6887831	.6529183	.6202426	.5836751	.5482697	.5142427	.4820806	.4502688
21	.4183780	.3890807	.3619186	.3363510	.3129186	.2913511	.2704322	.2529187	.2371349	.2226755
31	.2104592	.1994863	.1919728	.1859998	.1836214	.1852431	.1941620	.2117565	.2414862	.2850538
41	.3254051	.3689456	.3650807	.3236754	.2684862	.2185403	.1819458	.1558647	.1382701	.1261620
51	.1115675	.1107837	.1055134	.1005675	.0816756	.0548648	.0299459	.0162973	7.4054E-03	3.7297E-03
HEMP X										
	.2470000	.7630000	1.2460000	1.7280000	2.2120000	2.7000000	3.1950000	3.6870000	4.1870000	4.6920000
11	5.2030000	5.7190000	6.2410000	6.7690000	7.3020000	7.8420000	8.3880000	8.9400000	9.4980000	10.0610000
21	10.6300000	11.2040000	11.7840000	12.3680000	12.9560000	13.5490000	14.1460000	14.7460000	15.3500000	15.9600000
31	16.5650000	17.1770000	17.7900000	18.4040000	19.0190000	19.6340000	20.2460000	20.8550000	21.4570000	22.0520000
41	22.6370000	23.2170000	23.7980000	24.3870000	24.9840000	25.5940000	26.2100000	26.8330000	27.4590000	28.0900000
51	29.9880000	32.5280000	33.8010000	34.4390000	35.3680000	39.6190000	45.5830000	53.0370000	65.0770000	75.9950000
MOC P										
	1.0000000	.9853000	.9490000	.8932000	.8127000	.73805000	.671942000	.61438000	.5637000	.51884000
11	.0481000	.0343000	.0215000	.0163000	.0106000	6.1000E-03				
MOC X										
	0	1.0947400	2.0656550	3.0441900	6.4971930	9.4559120	13.0629660	14.6558000	29.1465000	30.7052980
11	34.3735660	40.3075140	46.0038450	54.9071890	65.9363680	87.1091730				

TABLE D-II

DATA FOR FIGS. 7, 8, AND 9

MOC T										
	5.6266E-03	.1505664	.3438540	.4634706	.6046533	.6779928	.8044836	.9072368	.9616311	1.0099900
11	1.0525529	1.1892277	1.3692442	1.5527802	1.6450199	1.7332010	1.8193604	1.8708493	1.9388722	1.9681061
21	2.1077312	2.2561775	2.3713311	2.6043342	2.7513127	2.8713637	3.0058968	3.1484124	3.2577402	3.4249069
31	3.5897973	3.7182350	3.9383434	4.0332040	4.1919540	4.4114184	4.5247000	4.5899373	4.6445413	4.7323779
41	4.7755999	4.9323281	5.0908684	5.2027722	5.2742097	5.5199876	5.7039579	5.8240388	5.9254740	5.9662398
51	5.9929727	6.0496135	6.0564877	6.1332269	6.2074949	6.2282972	6.3194885	6.4892163	6.6148534	6.6564279
61	6.6860363	6.7263378	6.8377624							
MOC X										
	4.6990E-03	.1261110	.2830830	.3776980	.4867910	.5421630	.6358890	.7120890	.7611110	.8192770
11	.8719820	1.0377170	1.2480290	1.4542770	1.5544800	1.6476980	1.7383760	1.7929860	1.8752820	1.9166840
21	2.1126450	2.3133050	2.4635460	2.7545030	2.9307790	3.0892750	3.2909510	3.4946590	3.6469320	3.8707060
31	4.0830500	4.2574210	4.5953680	4.7344330	4.9582070	5.2539900	5.4152800	5.5206900	5.6064150	5.7384950
41	5.8039000	6.0347860	6.2565280	6.4122300	6.5161160	6.9110860	7.1860410	7.3581260	7.5023980	7.5614530
51	7.6022200	7.6973430	7.7087730	7.8331060	7.9495650	7.9824580	8.1248250	8.3746340	8.5567520	8.6179660
61	8.6644480	8.7332820	8.9150190							
MOC U										
	.8397249	.8258898	.7958619	.7792970	.7590096	.7469798	.7284234	.7503239	1.0661125	1.2316379
11	1.2184852	1.1820672	1.1329927	1.0908669	1.0556276	1.0424749	1.0463215	1.0897502	1.3280496	1.4080825
21	1.3619861	1.3079484	1.2702274	1.1950958	1.1819431	1.5011440	1.4521316	1.3935029	1.3540448	1.2902667
31	1.2607352	1.5582218	1.4424532	1.4333332	1.3386587	1.3129116	1.6025811	1.5718708	1.4789954	1.4814150
41	1.4944436	1.3778065	1.3696792	1.3747045	1.6403640	1.5293727	1.4160858	1.4034295	1.4024368	1.4551096
51	1.5321025	1.6370138	1.6419771	1.5394233	1.5451311	1.5586560	1.5113808	1.4332712	1.4232826	1.4806085
61	1.6862123	1.6622845	1.5662250							
MAGEE COARSE T										
	6.3500E-03	.1333500	.2603500	.3873500	.5143500	.6413500	.7683500	.8953500	1.0223500	1.1493500
11	1.2763500	1.4033500	1.5303500	1.6573500	1.7843500	1.9113500	2.0383500	2.1653500	2.2923500	2.4193500
21	2.5463500	2.6733500	2.8003500	2.9273500	3.0543500	3.1813500	3.3083500	3.4353500	3.5623500	3.6893500
31	3.8163500	3.9433500	4.0703500	4.1973500	4.3243500	4.4513500	4.5783500	4.7053500	4.8323500	4.9593500
41	5.0863500	5.2133500	5.3403500	5.4673500	5.5943500	5.7213500	5.8483500	5.9753500	6.1023500	6.2293500
51	6.3563500	6.4833500	6.6103500	6.7373500	6.8643500	6.9913500	7.1183500	7.2453500		
MAGEE COARSE X										
	.0552450	.1109980	.1957070	.3054350	.4279900	.5483860	.6568440	.7539990	.8501380	.9597390
11	1.0918190	1.2434570	1.4030960	1.5593060	1.7086580	1.8543270	2.0010120	2.1499830	2.2993350	2.4494490
21	2.6054050	2.7748230	2.9579570	3.1449010	3.3215580	3.4809430	3.6295330	3.7832030	3.9546530	4.1432480
31	4.3370500	4.5241210	4.7020480	4.8759110	5.0506630	5.2268850	5.4029610	5.5822850	5.7710070	5.9706510
41	6.1729620	6.3646050	6.5401190	6.7090290	6.8883530	7.0872350	7.2981820	7.5043030	7.6962000	7.8781910
51	8.0618330	8.2546190	8.4548980	8.6574630	8.8581230	9.0570050	9.2609670			
MAGEE COARSE U										
	.3267000	.5687000	.7719000	.9320000	.9749000	.9074000	.8033000	.7423000	.7914000	.9428000
11	1.1242000	1.2375000	1.2547000	1.2038000	1.1544000	1.1445000	1.1651000	1.1767000	1.1753000	1.1968000
21	1.2677000	1.3915000	1.4746000	1.4512000	1.3251000	1.1970000	1.1639000	1.2708000	1.4244000	1.5228000
31	1.5119000	1.4362000	1.3755000	1.3670000	1.3810000	1.3849000	1.3922000	1.4432000	1.5301000	1.5972000
41	1.5682000	1.4470000	1.3371000	1.3504000	1.4825000	1.6281000	1.6626000	1.5688000	1.4602000	1.4262000
51	1.4795000	1.5505000	1.5913000	1.5873000	1.5721000	1.5774000	1.6440000	1.7272000		
MAGEE FINE T										
	.0240170	.1510170	.2780170	.4050170	.5320170	.6590170	.7860170	.9130170	1.0400170	1.1670170
11	1.2940170	1.4210170	1.5480170	1.6750170	1.8020170	1.9290170	2.0560170	2.1830170	2.3100170	2.4370170
21	2.5640170	2.6910170	2.8180170	2.9450170	3.0720170	3.1990170	3.3260170	3.4530170	3.5800170	3.7070170
31	3.8340170	3.9610170	4.0880170	4.2150170	4.3420170	4.4690170	4.5960170	4.7230170	4.8500170	4.9770170
41	5.1040170	5.2310170	5.3580170	5.4850170	5.6120170	5.7390170				

TABLE D-II (cont)

MAGEE FINE X										
	.0414020	.1252220	.2537460	.3726180	.4561840	.5400040	.6502400	.7608570	.8663940	.9999980
11	1.1597640	1.3147040	1.4635480	1.6089630	1.7392650	1.8703290	2.0289520	2.1963380	2.3548340	2.5243790
21	2.7066240	2.8737560	3.0204410	3.1681420	3.3387030	3.5255200	3.7059870	3.8854380	4.0673020	4.2341800
31	4.4005500	4.5740320	4.7459900	4.9472850	5.1554380	5.3216810	5.4937660	5.6843930	5.8544460	6.0425330
41	6.2496700	6.4452500	6.6357500	6.8136770	6.9917310	7.1869300				
MAGEE FINE U										
	.4220000	.8843000	1.0456000	.7963000	.5966000	.7690000	.9139000	.8187000	.9013000	1.1959000
11	1.2654000	1.1780000	1.1719000	1.0805000	1.0318000	1.1295000	1.3302000	1.2748000	1.2556000	1.4139000
21	1.4095000	1.2199000	1.1238000	1.2336000	1.4377000	1.4617000	1.3918000	1.4417000	1.3836000	1.2729000
31	1.3577000	1.3448000	1.4265000	1.6903000	1.4745000	1.2336000	1.4921000	1.4221000	1.3409000	1.6134000
41	1.5922000	1.5148000	1.4635000	1.3592000	1.4758000	1.5712000				
HEMP X										
	5.0000E-03	.0640000	.1820000	.2830000	.3770000	.4870000	.6360000	.7300000	.8730000	.9780000
11	1.1380000	1.2490000	1.3530000	1.5340000	1.6470000	1.7670000	1.8760000	2.0080000	2.1580000	2.3130000
21	2.4640000	2.6100000	2.7550000	2.8930000	3.0150000	3.1500000	3.2910000	3.4950000	3.6480000	4.4170000
HEMP T										
	-.0970000	.0780000	.2130000	.3230000	.4480000	.5930000	.7780000	.8980000	1.0540000	1.1530000
11	1.2880000	1.3760000	1.4600000	1.6190000	1.7220000	1.8300000	1.9270000	2.0390000	2.1610000	2.2800000
21	2.3870000	2.4910000	2.6000000	2.7070000	2.8030000	2.9110000	3.0220000	3.1710000	3.2790000	3.8220000
MOC DEL T										
	2.0120E-03	.0535599	.1260978	.1729337	.2301987	.2609443	.3153382	.3594760	.3761611	.3797769
11	.3817976	.3909839	.4092219	.4341056	.4492661	.4657410	.4821481	.4916293	.4963475	.4937338
21	.4826197	.4767121	.4762957	.4854857	.4966673	.4949983	.4743960	.4602131	.4524079	.4474408
31	.4489896	.4432958	.4034449	.3813325	.3779486	.3698876	.3591000	.3432526	.3319143	.3181510
41	.3110614	.2901850	.2781545	.2702875	.2618127	.2037676	.1762340	.1639419	.1543987	.1497375
51	.1451112	.1285805	.1266623	.1077607	.0924449	.0879449	.0696232	.0471901	.0327365	.0272233
61	.0210763	8.4286E-03	-.0199446							
MAGEE COARSE DEL T										
	-.0361462	.0479669	.1098062	.1524000	.1851269	.2195146	.2630854	.3153508	.3683977	.4110892
11	.4364892	.4468446	.4510454	.4578838	.4699977	.4849446	.4991100	.5115169	.5236308	.5351585
21	.5421923	.5388708	.5249985	.5081954	.4993054	.5037015	.5164015	.5251938	.5203092	.5022362
31	.4801577	.4632569	.4533900	.4466492	.4392246	.4308231	.4222262	.4112846	.3931138	.3665415
41	.3379177	.3175000	.3094892	.3065585	.2956169	.2696308	.2343638	.2028092	.1821962	.1692031
51	.1549400	.1336431	.1065823	.0777631	.0504092	.0244231	-5.4708E-03	-.0453292		
MAGEE FINE DEL T										
	-7.8307E-03	.0546924	.0828277	.1183877	.1811062	.2436293	.2858324	.3277424	.3735600	.3977877
11	.4018908	.4097062	.4222108	.4373531	.4641208	.4903024	.4952847	.4935262	.4986062	.4951870
21	.4819985	.4804354	.4946008	.5079847	.5037839	.4870785	.4752577	.4642185	.4513231	.4499554
31	.4489785	.4425308	.4372554	.4094131	.3762954	.3754162	.3700431	.3504070	.3465970	.3289147
41	.2965785	.2731324	.2535939	.2437270	.2337624	.2106093				
HEMP DELT										
	-.1008462	.0287692	.0730000	.1053077	.1580000	.2183846	.2887692	.3384615	.3824615	.4006923
11	.4126154	.4152308	.4192308	.4390000	.4550769	.4707692	.4839231	.4943846	.5010000	.5007692
21	.4916154	.4833077	.4807692	.4816154	.4837692	.4879231	.4904615	.4825385	.4728462	.4243077





TABLE D-III (cont)

HEMP DEL T										
	0	-.0146603	-.0250118	-.0716169	-.0940284	-.1028065	-.1038782	-.1015054	-.0902091	-.0747988
11	-.0609651	-.0476411	-.0362337	-.0277766	-.0200348	-.0145772	-9.8289E-03	-6.1065E-03	-5.6551E-03	-2.6487E-03
21	2.7754E-03									
LLL EXPT T										
	0	1.1000000	1.8700000	2.6000000	3.2700000	3.9300000	4.5600000	5.1810000	5.7900000	6.3900000
11	6.9800000	7.5700000	8.1500000	8.7300000	9.3000000	9.8700000	10.4400000	11.0000000	11.5600000	12.1300000
21	12.6800000									
LLL EXPT X										
	0	1.0000000	2.0000000	3.0000000	4.0000000	5.0000000	6.0000000	7.0000000	8.0000000	9.0000000
11	10.0000000	11.0000000	12.0000000	13.0000000	14.0000000	15.0000000	16.0000000	17.0000000	18.0000000	19.0000000
21	20.0000000									
LLL EXPT DEL T										
	0	.0493397	-.0450118	-.0776169	-.1060284	-.1078065	-.1098782	-.1015054	-.0912091	-.0797988
11	-.0709651	-.0566411	-.0482337	-.0367766	-.0330348	-.0275772	-.0208289	-.0231085	-.0246551	-.0156487
21	-.0262246									
LASL EXPT T										
	0	1.1541700	1.9704500	2.6735800	3.3487000	4.0240400	4.6431400	5.2904700	5.8815600	6.5004400
11	7.0913000	7.6539000	8.2448000	8.8355000	9.3983000	9.9612000	10.5240000	11.0870000	11.6500000	12.2120000
21	12.7750000	13.3380000	13.8730000							
LASL EXPT X										
	0	1.0357100	2.0232900	3.0185800	4.0119400	5.0322500	6.0121300	7.0603500	8.0325300	9.0701700
11	10.0660000	11.0160000	12.0240000	13.0480000	14.0350000	15.0190000	16.0070000	17.0050000	18.0040000	19.0070000
21	20.0170000	21.0300000	22.0030000							
LASL EXPT DEL T										
	0	.0701619	.0367265	-.0175318	-.0374138	-.0345292	-.0342725	-.0285170	-.0189380	-.0103554
11	2.1889E-03	.0180845	.0328891	.0414960	.0454801	.0529102	.0592320	.0610821	.0630999	.0624260
21	.0592486	.0547110	.0448128							
MAGEE T										
	0	.7800000	.8800000	.9800000	1.0800000	1.1800000	1.2800000	1.3800000	1.4800000	1.5800000
11	.7800000	.8800000	.9800000	1.0800000	1.1800000	1.2800000	1.3800000	1.4800000	1.5800000	1.6800000
21	1.7800000	1.8800000	1.9800000	2.0800000	2.1800000	2.2800000	2.3800000	2.4800000	2.5800000	2.6800000
31	2.7800000	2.8800000								
MAGEE X										
	0	.0143000	.0303100	.0585500	.1033900	.1676400	.2506600	.3476900	.4507900	.5515800
11	.7277900	.8060500	.8861700	.9755600	1.0789600	1.1963800	1.3237400	1.4549500	1.5850200	1.7119100
21	1.8365400	1.9610900	2.0871600	2.2145700	2.3418900	2.4680600	2.5943700	2.7246800	2.8637000	3.0133000
31	3.1709000	3.3295000								
LASL EXPT T										
	0	.0286700	.0566800	.0846900	.1129200	.1411600	.1691700	.1971800	.2254100	.2534200
11	.2814300	.3096600	.3378900	.3661200	.3943500	.4223600	.4506000	.4788300	.5070600	.5352900
21	.5633000	.5915300	.6195400	.6479900	.6757800	.7040100	.7320200	.7602600	.7882700	.8162800
31	.8442900	.8723000	.9005300	.9287600	.9567700	.9850000	1.0134500	1.0414600	1.0697000	1.0979300
41	1.1259400	1.1541700	1.1824000	1.2104100	1.2386400	1.2668700	1.2951000	1.3231100	1.3511200	1.3791400
51	1.4073700	1.4356000	1.4638100	1.4918200	1.5196300	1.5476600	1.5756700	1.6041000	1.6321100	1.6605600
61	1.6888000	1.7170300	1.7450400	1.7732700	1.8015000	1.8297300	1.8577400	1.8859700	1.9139800	1.9422100
71	1.9704500	1.9982400	2.0264700	2.0544800	2.0827100	2.1107200	2.1389500	2.1667400	2.1949700	2.2232000
81	2.2512100	2.2794400	2.3076800	2.3359100	2.3641400	2.3923700	2.4203800	2.4486100	2.4768400	2.5050700
LASL EXPT X										
	0	.0288800	.0567900	.0848200	.11010700	.1299500	.1530500	.1800000	.2069500	.2300500
11	.2550800	.2822900	.3080200	.3291900	.3523000	.3725100	.3965000	.4216000	.4418100	.4658800
21	.4889800	.5130400	.5342200	.5534700	.5775300	.6016000	.6237400	.6429900	.6651300	.6901500
31	.7151800	.7373200	.7594600	.7767800	.7989200	.8249100	.8557100	.8884400	.9221300	.9596700
41	.9924000	1.0357100	1.0655500	1.1079000	1.1435200	1.1800900	1.2176300	1.2551700	1.2927100	1.3273700
51	1.3561700	1.3995600	1.4265100	1.4573100	1.4881100	1.5256500	1.5603000	1.5968800	1.6226700	1.6566000
61	1.6821700	1.7210500	1.7537800	1.7893900	1.8211600	1.8615800	1.8914200	1.9203000	1.9568800	1.9876200
71	2.0232900	2.0608300	2.0945200	2.1320600	2.1753800	2.2167700	2.2533400	2.3043600	2.3351600	2.3733600
81	2.4150500	2.4564400	2.4978300	2.5401900	2.5796500	2.6210400	2.6653200	2.7038200	2.7442500	2.7796600

REFERENCES

1. J. W. Kury, H. C. Hornig, E. L. Lee, J. L. McDonnell, D. L. Ornellas, M. Finger, F. M. Strange, and M. L. Wilkins, "Metal Acceleration in Chemical Explosives," in Fourth Symposium (International) on Detonation, ACR-126, Office of Naval Research, Arlington, VA, 1965, pp. 3-13.
2. M. Finger, H. C. Hornig, E. L. Lee, and J. W. Kury, "Metal Acceleration by Composite Explosives," in Fifth Symposium (International) on Detonation, ACR-184, Office of Naval Research, Arlington, VA, 1970, pp. 137-152.
3. M. L. Wilkins, "The Use of One- and Two-Dimensional Hydrodynamic Machine Calculations in High Explosive Research," in Fourth Symposium (International) on Detonation, ACR-126, Office of Naval Research, Arlington, VA, 1965, pp. 519-526.
4. N. E. Hoskin, J. W. S. Allan, W. A. Bailey, J. W. Lethaby, and I. C. Skidmore, "The Motion of Plates and Cylinders Driven by Detonation Waves at Tangential Incidence," in Fourth Symposium (International) on Detonation, ACR-126, Office of Naval Research, Arlington, VA, 1965, pp. 14-26.
5. M. L. Wilkins, "Calculation of Elastic-Plastic Flow," Lawrence Livermore Laboratory report UCRL-7322, Rev. I (January 1969).
6. A. W. Campbell and R. P. Engelke, Los Alamos Scientific Laboratory, personal communication, 1974.
7. E. L. Lee, H. C. Hornig, and J. W. Kury, "Adiabatic Expansion of High Explosive Detonation Products," Lawrence Radiation Laboratory report UCRL-50422 (May 1968).
8. D. Venable and E. Sandoval, Los Alamos Scientific Laboratory, personal communication, 1974.
9. D. H. Edwards, T. G. Jones, and B. Prince, "Observations on Oblique Shock Waves in Gaseous Detonations," *J. Fluid Mech.* 17, 21-32 (1963).
10. C. L. Mader, "The Two-Dimensional Hydrodynamic Hot Spot, Volume III," Los Alamos Scientific Laboratory report LA-3450 (April 1966). The original 2DL code described here has undergone additional development.
11. James D. Kershner and C. L. Mader, "2DE: A Two-Dimensional Continuous Eulerian Hydrodynamic Code for Computing Multicomponent Reactive Hydrodynamic Problems," Los Alamos Scientific Laboratory report LA-4846 (March 1972).
12. P. L. Browne and M. S. Hoyt, "HASTI - A Numerical Calculation of Two-Dimensional Lagrangian Hydrodynamics Utilizing the Concept of Space-Dependent Time Steps," Los Alamos Scientific Laboratory report LA-3324-MS (May 1965).
13. W. Herrmann, "Comparison of Finite Difference Expressions Used in Lagrangian Fluid Flow Calculations," Air Force Weapons Laboratory report WL-TR-64-104 (November 1964).
14. M. L. Wilkins, "Calculation of Elastic-Plastic Flow," *Methods Comput. Phys.* 3, 211-262 (1964).
15. M. L. Wilkins, "The Equation of State of PBX 9404 and LX04-01," Lawrence Livermore Laboratory report UCRL-7797 (April 1964).